Frequency-swept Ferromagnetic Resonance Characterization of Permalloy Thin Films

Samuel Holladay

Electrical Engineering and Computer Sciences
University of California at Berkeley

Technical Report No. UCB/EECS-2018-53
http://www2.eecs.berkeley.edu/Pubs/TechRpts/2018/EECS-2018-53.html

May 11, 2018

Copyright © 2018, by the author(s).
All rights reserved.

Permission to make digital or hard copies of all or part of this work for personal or classroom use is granted without fee provided that copies are not made or distributed for profit or commercial advantage and that copies bear this notice and the full citation on the first page. To copy otherwise, to republish, to post on servers or to redistribute to lists, requires prior specific permission.

Frequency-swept Ferromagnetic Resonance Characterization of Permalloy Thin Films

by Samuel Holladay

Research Project

Submitted to the Department of Electrical Engineering and Computer Sciences, University of California at Berkeley, in partial satisfaction of the requirements for the degree of **Master of Science, Plan II**.

Approval for the Report and Comprehensive Examination:

Committee:

Professor Sayeef Salahuddin
Research Advisor

(Date)

* * * * * * *

Professor Jeffrey Bokor
Second Reader

(Date)

Abstract

The dynamic properties of permalloy thin films were studied with vector network analyzer based ferromagnetic resonance (VNA-FMR). Resonance was excited in the magnetic samples with coplanar waveguides (CPWs), and the resulting absorption change was analyzed in the frequency domain to yield the magnetization and damping of the measured samples. Two different VNA-FMR setups are discussed: one system uses a flip-chip geometry in which the magnetic sample is placed on top of a relatively large CPW, while the other uses a microwave probe station to contact smaller CPWs that were deposited and lithographically patterned on top of the magnetic sample. The flip-chip setup is shown to be capable of conducting broadband, frequency-swept FMR measurements in the in-plane (IP) and out-of-plane (OOP) orientations, and is validated with measurements of permalloy (Py) thin films. A transition from IP to OOP resonance is observed by applying a high magnetic field along the Py sample's hard axis. Finally, the microwave probe setup is evaluated. The method for fabricating CPWs with photolithography and thermal evaporation is discussed, and shown to yield waveguides with low loss and good broadband performance. FMR signals are found to be weaker in this measurement setup due to the smaller change in absorption associated with the smaller device geometries, and it is shown that the strength of the FMR signal is relatively uncorrelated with high-frequency losses in the system.

Acknowledgments

I would first like to thank my advisor, Sayeef Salahuddin, for his guidance and support throughout my undergraduate and graduate career at Berkeley. Professor Salahuddin provided me with the opportunity to do device research when I was still deciding whether to pursue electrical engineering or computer science, and his vast expertise and the conviction of his ideas have been a source of inspiration to me ever since. I further thank him for agreeing to take me on as a Master's student at Berkeley, giving me one more year in my favorite college home. I would also like to thank Professor Jeffrey Bokor for being the second reader on this master's report. In addition, I want to recognize some of the great professors I have had at Berkeley who have challenged me and taught me, inside and outside of the classroom, professors like Vivek Subramanian, Ali Niknejad, Kristofer Pister, and Irfan Siddiqi.

Next, I want to thank the other graduate students who helped me with my research, providing mentorship to me as an undergraduate and camaraderie as a graduate student. I thank Praveen Gowtham for his many deep insights into device physics, Niklas Roschewsky for his part in getting the experimental setup operational, Dominic Labanowski for his knowledge of ferromagnetic resonance and experimental design, Adi Jung and Ava Tan for assistance in device fabrication, Korok Chatterjee for his unique career and rock-climbing advice, and Saavan Patel for his social enthusiasm, for helping me pass many classes, and for his purchase of a highly appreciated group coffee machine. (He was also a very good roommate). I appreciate the environment that the entire group brought that helped me survive the difficult times that every researcher faces. I also thank the admin and staff in the EECS department, Nanolab, and Berkeley administration who have helped me along my journey.

Finally, I would like to thank my family, who have always been my source of strength and motivation. My older siblings Ben and Annie and my twin sister Rachel helped make me the person I am today, and were always a source of comfort in college even if they were many miles away. And of course, I thank my parents, Ken and Wendy, who have supported me, loved me, encouraged me, and understood me, giving me the freedom to move away and follow my dreams while keeping me steady along the paths I choose. I owe any success I may have achieved to them, and they have given me an example for how to live my life. I just hope my Mom will be pleased to have another engineer in the family. I owe many people for this degree, but her most of all.

Contents

Chapter 1

Introduction

As electronics continue to be scaled in size and power consumption, while demanding ever higher performance, the industry has started to reach the limits of conventional electronic techniques. A wide variety of emerging technologies aim to manipulate novel materials, utilize new geometries, and exploit hitherto underused physical phenomena to create new classes of efficient hardware.

Spintronics is a research area which aims to exploit the spin degree of freedom of electrons to develop new electronic devices, particularly in the field of memory. Spin describes the intrinsic angular momentum of a particle, which produces a magnetic dipole moment. In most materials, without an external magnetic field to align the spins no large-scale spin order exists. However, in ferromagnetic and ferrimagnetic materials a spontaneous magnetic order exists even in the absence of an applied magnetic field due to the presence of an exchange interaction which tends to align neighboring spins. Magnetic materials are thus of interest for use in spintronic devices due to their spin polarization, which can be used to produce spin-polarized currents. A thorough understanding of the properties of a material is needed to adapt it to application in spintronic hardware. One important technique to measure the bulk spin properties of ferromagnetic materials and thin films is ferromagnetic resonance (FMR), and the primary focus of this report is the development of techniques to measure FMR and characterize a multifaceted experimental FMR setup.

This chapter gives an overview of the theoretical background of ferromagnetic resonance, its application to electronic devices and usefulness as a spectroscopic technique, and the analysis of FMR signals. Section 1.1 establishes the motivation for this research in the context of spintronic applications, and briefly outlines current research in spin transport and spin dynamics. Section 1.2 explains the theoretical background behind ferromagnetic resonance, and derives the fundamental equations used to describe FMR and extract material properties from the resulting resonant signal. Section 1.3 describes the analysis of FMR signals in the frequency domain as produced by frequency-swept FMR, which is an alternative to the more typical field-swept FMR.

1.1 Spintronics

All elementary particles carry intrinsic angular momentum, denoted by the quantum spin operator $\boldsymbol{S}$. A given particle has a specific value of spin, described by the spin quantum number s. The spin quantum number is quantized in half-integer steps of the reduced Planck constant $\hbar = 1.054 \times 10^{-34}$ J-s. In electronics and spintronics we consider the electron, with a charge of $-e$ and a spin quantum number of 1/2.

The spin $\boldsymbol{S}$ of the electron is an operator described by[1]

$$\boldsymbol{S} = \frac{\hbar}{2}\boldsymbol{\sigma} \tag{1.1}$$

where $\boldsymbol{\sigma}$ is the Pauli spin matrix. The eigenvalues of the Pauli spin matrix are $\frac{\hbar}{2}$ and $-\frac{\hbar}{2}$, which describe the two possible values of the spin operator for electrons. These spin states are also known as spin up ($|\uparrow\rangle$) or down ($|\downarrow\rangle$).

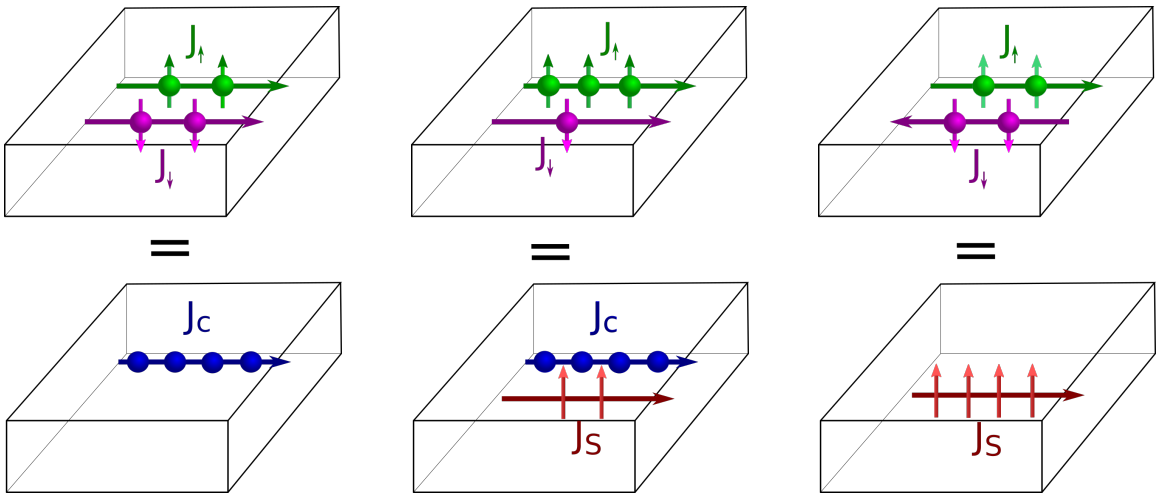

Figure 1.1: **(a)** Pure charge current. **(b)** Spin-polarized current. **(c)** Pure spin current.

Since all the electrons in a charge current have spin up or down, the density $\boldsymbol{J}_C$ is simply given in terms of the spin up current density $\boldsymbol{J}_\uparrow$ and spin down current density $\boldsymbol{J}_\downarrow$ as

$$\boldsymbol{J}_C = \boldsymbol{J}_\uparrow + \boldsymbol{J}_\downarrow \tag{1.2}$$

while the equivalent spin current density $\boldsymbol{J}_s$ is given by[2]

$$\boldsymbol{J}_s = -\frac{\hbar}{2e}(\boldsymbol{J}_\uparrow - \boldsymbol{J}_\downarrow) \tag{1.3}$$

In typical charge currents, equal numbers of spin up and spin down electrons exist, so it can be seen from Eq. 1.3 that there is no net spin polarization (Fig. 1.1a). However,

if $\boldsymbol{J}_\uparrow > \boldsymbol{J}_\downarrow$, then both spin and charge are transported in a so-called spin-polarized current (Fig. 1.1b). In the case that the current densities are equal in magnitude but have opposite direction ($\boldsymbol{J}_\uparrow = -\boldsymbol{J}_\downarrow$), a pure spin current is created where no net charge flows (Fig. 1.1c).

Spintronics can be viewed as an analog to conventional electronics, with spin-polarized or pure spin currents being manipulated with magnetic fields in the same way that charge currents are manipulated with electric fields. Spintronics has found widespread adoption particularly in memory applications, with the discovery of giant magnetoresistance in the 1980s being applied in hard disk drive read heads and leading to the 2007 Nobel Prize in Physics being awarded to the discoverers of this phenomenon, Albert Fert and Peter Grunberg. More recent research has focused on new forms of low-power, non-volatile solid-state memory such as racetrack memory or magnetoresistive RAM (MRAM)[3]. MRAM holds the possibility of being a "universal memory," with the advantages of nonvolatility and competitive read/write times. One of its main disadvantages, however, is the relatively large amount of power needed to switch the magnetization of a memory cell for a read/write operation, due to the need to use current pulses that generate magnetic fields using the Oersted effect. Research is active into determining lower power ways to switch magnetization, such as spin-transfer torque (STT)[4].

Characterizing the bulk and interface spin transport properties of new materials is especially important to determine these lower power switching techniques for memory applications. In particular, since pure spin currents tend to decohere over a given spin-flip relaxation rate due to damping[5], materials used in spintronic devices such as spin transistors[6] or spin valves[7] require analysis of their damping characteristics. For this purpose, ferromagnetic resonance has been used as a spectroscopic technique for probing the dynamic properties of magnetic materials for decades.

1.2 Ferromagnetic resonance theory

The spin of a charged particle produces a magnetic dipole with dipole moment

$$\mu = \gamma \boldsymbol{S} \tag{1.4}$$

where $\boldsymbol{S}$ is the spin of the particle and γ is the gyromagnetic ratio[1]. An electron with spin 1/2 has a magnetic dipole moment of $\mu_B = 9.274 \times 10^{-24}$ J/T, the Bohr magneton, described by $\mu_B = \frac{e\hbar}{2m_e}$. For a free electron, the gyromagnetic ratio and Bohr magneton are related by $\gamma = g\frac{\mu_B}{\hbar}$, where g is the dimensionless Landé g-factor (approximately 2 for electrons).

The Hamiltonian of an electron in an external magnetic field oriented in the z-direction $\boldsymbol{B} = \boldsymbol{B}_0\hat{z}$ is

$$\hat{H} = \gamma \boldsymbol{B}_0 \boldsymbol{S}_z \tag{1.5}$$

The dipole moment produced by the spin, tilted at an angle to $\boldsymbol{B}_0$, will precess about the magnetic field at the Larmor frequency $\omega = \gamma \boldsymbol{B}_0$. However, in ferromagnetic materials,

the exchange interaction couples the magnetic moments so that all the individual spins are considered one macrospin with magnetization $\boldsymbol{M}$ [2].

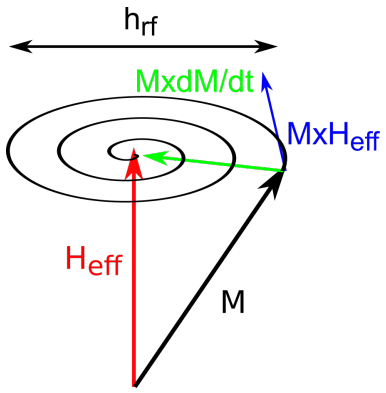

Figure 1.2: Illustration of the precession of $\boldsymbol{M}$ about the effective magnetic field $\boldsymbol{H}_{eff}$, shown in red. The torque produced by $\boldsymbol{H}_{eff}$ on $\boldsymbol{M}$ is shown in blue. The tickle field $\boldsymbol{h}_{rf}$, shown in black, excites the damped precession, which is the torque term shown in green, causing the spiral motion of the magnetization in towards $\boldsymbol{H}_{eff}$.

The magnetization dynamics of a spin precessing in a magnetic field are described by the Landau-Lifshitz-Gilbert (LLG) equation [8]:

$$\frac{d\boldsymbol{M}}{dt} = \gamma \boldsymbol{M} \times \boldsymbol{H_{eff}} - \frac{\alpha}{\boldsymbol{M}_s} \boldsymbol{M} \times \frac{d\boldsymbol{M}}{dt} \tag{1.6}$$

where $\boldsymbol{M}_s$ is the saturation magnetization, α is the Gilbert damping parameter, and $\boldsymbol{H}_{eff}$ is the effective magnetic field, taking the form

$$\boldsymbol{H}_{eff} = \boldsymbol{H}_0 + \boldsymbol{H}_{ani} + \boldsymbol{H}_{demag} \tag{1.7}$$

$\boldsymbol{H}_{eff}$ is the combination of the external magnetic field $\boldsymbol{H}_0 = \mu_0 \boldsymbol{B}_0$, the anisotropy $\boldsymbol{H}_{ani}$, and the demagnetization field $\boldsymbol{H}_{demag}$. This is also called shape anisotropy, and it is specific to the shape of a sample. [9]

The first term on the right hand side of the LLG equation describes the torque acting to align the magnetization about the effective field, while the second term describes the dissipation of the magnetization precession governed by the Gilbert damping factor α, which causes the spin to spiral in towards the external field until it is aligned with $\boldsymbol{H}_{eff}$, as seen in Fig. 1.2.

To reach ferromagnetic resonance, an applied magnetic "tickle field" $\boldsymbol{h}_{rf} = \boldsymbol{h}e^{i\omega t}$, produced by an RF current at the frequency $\omega = 2\pi f$ due to the Oersted effect, excites the precession of this macrospin around $\boldsymbol{H}_{eff}$.

Energy is strongly absorbed from the RF magnetic field when its frequency is $f = f_0$, the resonant frequency of the precessing spins, causing a change in the RF current's absorption that can be observed as a change in signal transmission. The motion of a damped precessing

spin is similar to that of a damped harmonic oscillator. In the frequency domain, this resonant absorption can be modeled as a complex Lorentzian peak at the resonant frequency f_0 with a full width at half maximum (FWHM) of Δf. The real component of the absorption behaves like a symmetric Lorentzian, while the imaginary component is an asymmetric Lorentzian.

By analyzing the shape of the resonant absorption, one can use FMR to extract $\boldsymbol{M}_s$ and α, important parameters for characterizing magnetic materials for spintronics applications. The Gilbert damping constant α is a phenomenological term that controls the magnetization relaxation rate[10], and can also be written as $\alpha = \frac{\lambda}{\gamma \boldsymbol{M}}$ [11], where λ is the relaxation length introduced by Landau and Lifshitz[12]. Gilbert damping is generally believed to be produced by spin-orbit interaction, which couples the ferromagnet's spin to its lattice[13]. This affects domain-wall velocity[14] and spin current dynamics, which makes it particularly relevant for characterizing materials for spintronic device applications.

The resonant frequency of a precessing magnet can be found by linearizing the LLG equation and solving for a static field B_0 in the $\mathbf{z}$ direction. In this situation, the components of the magnetic field within the sample are given by

$$B_x = B_x^0 - N_x \mu_0 M_x \tag{1.8a}$$
$$B_y = B_y^0 - N_y \mu_0 M_y \tag{1.8b}$$
$$B_z = B_z^0 - N_z \mu_0 M_z \tag{1.8c}$$

where N_x, N_y, and N_z are the demagnetization factors of the sample.

Kittel[15] uses the simplified equation of motion $\frac{d\boldsymbol{M}}{dt} = \gamma \boldsymbol{M} \times \boldsymbol{H_{eff}}$, and sets $\frac{d\boldsymbol{M}_z}{dt} = 0$ and $\boldsymbol{M}_z = \boldsymbol{M}$ to derive the namesake equation which describes the fundamental mode for the resonant frequency f_{res} in the applied field B_0:

$$f_{res}^2 = \gamma^2 [B_0 + (N_y - N_z)\mu_0 M][B_0 + (N_x - N_z)\mu_0 M] \tag{1.9}$$

For a magnetic thin film with $N_x = 0$, the expression for f_{res} simplifies to two forms based on the orientation of the applied magnetic field. In the in-plane orientation, the field is parallel to the plane of the film, so that $N_x = N_z = 0$ and $N_y = 1$. In the out-of-plane orientation, the field is perpendicular to the plane of the film, so that $N_x = N_y = 0$ and $N_z = 1$.. The dependence of f_{res} on the magnetic field is thus

$$f_{res} = \gamma \sqrt{B_0(B_0 + \mu_0 M)} \qquad \text{(In-plane magnetic field)} \tag{1.10a}$$
$$f_{res} = \gamma (B_0 - \mu_0 M) \qquad \text{(Out-of-plane magnetic field)} \tag{1.10b}$$

1.3 Frequency-swept FMR

The resonant frequency depends on both frequency and magnetic field, so both parameters must be swept in FMR. In typical field-swept FMR, the frequency is held constant and the magnetic field is swept. The measurement is then repeated for a range of frequencies in order to obtain f_{res} as a function of both f and $\boldsymbol{B}$. However, in this thesis a frequency-swept FMR technique was used, in which the frequency was swept with a vector network analyzer (method described in chapter 2) at a constant magnetic field, with the measurement then repeated for a range of magnetic fields. This technique has the advantage of allowing rapid, broadband FMR measurements by using the VNA rather than field modulation, but it requires a different analysis of the resonant signal, which is produced in the frequency domain rather than the field domain.

The typical Gilbert damping model relates the damping constant α to the full-width half-maximum (FWHM) of the resonance peak, swept in the field domain, as [5]

$$\Delta H = \Delta H_0 + \frac{4\pi\alpha f}{|\gamma|} \tag{1.11}$$

Here ΔH_0 describes the inhomogeneous broadening that is a result of sample imperfections. It is ideally zero for a perfect sample, and since it is intrinsic to the sample being measured it is clearly independent of frequency.

In order to extract α from the frequency linewidth Δf, as found in frequency-swept VNA-FMR, the field linewidth must be converted into a frequency linewidth by differentiating the Kittel equation (Eq. 1.9), which fundamentally relates the frequency and field at resonance [16] [17]:

$$\Delta f = \Delta H \frac{\partial f_{Kittel}(H_{eff})}{\partial H_{eff}}\bigg|_{H_{eff}=H_{Kittel}(f)} \tag{1.12}$$

Based on the Kittel equation, the frequency linewidth for an out-of-plane magnetized film is a linear function of f_{res}:

$$\Delta f = 2\alpha f_{res} + \gamma\mu_0\Delta H_0 \tag{1.13}$$

The characteristic square-root dependence of the resonant frequency on the magnetic field for in-plane magnets produces an inverse square-root shape for the frequency linewidth [18]:

$$\Delta f = (2\alpha f_{res} + \gamma\mu_0\Delta H_0)\sqrt{1 + (\frac{\gamma\mu_0 M_s}{2f_{res}})^2} \tag{1.14}$$

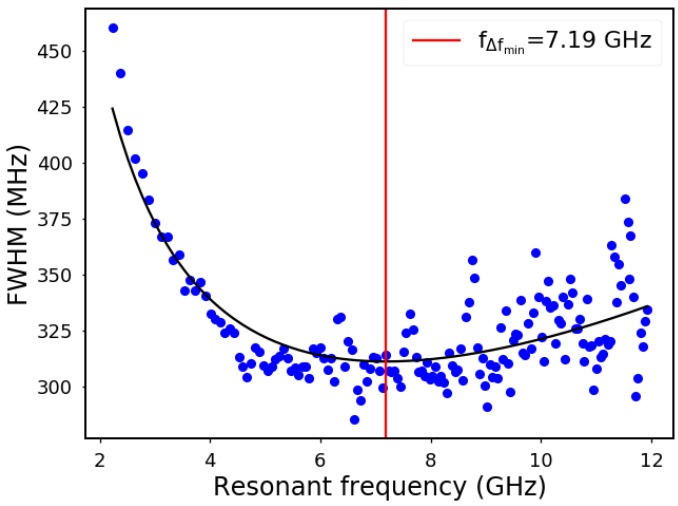

Figure 1.3: The extracted frequency linewidth Δf vs extracted resonant frequency f_{res} for a 30 nm permalloy film in the in-plane configuration. The blue dots indicate the extracted linewidths for each frequency sweep, while the black line shows the fit to Eq. 1.14, displaying the characteristic inverse square-root dependence of Δf vs f_{res}. The red line indicates the location of the minimum linewidth at an intermediate frequency $f_{\Delta f_{min,IP}}$.

As seen in Figure 1.3, the in-plane frequency linewidth is very large at low resonant frequencies, and then decreases until hitting a minimum at

$$f_{\Delta f_{min,IP}} = \frac{\mu_0 \gamma}{2} \left(\frac{\Delta H_0 M_s^2}{\alpha}\right)^{\frac{1}{3}} \tag{1.15}$$

After this frequency $f_{\Delta f_{min,IP}}$, the linewidth tends to increase again, albeit slowly. The increased linewidth at lower frequencies is an artifact of the measurement technique resulting from the square-root shape of the in-plane Kittel equation, and does not imply enhanced damping[19] [20].

Chapter 2

FMR measurement, signal analysis, and design techniques

In this chapter the details of conducting general FMR measurements and analyzing FMR data are discussed, and the methods of fitting the signal to the models found in Chapter 1 are discussed.

First, the design and optimization of coplanar waveguides is discussed. Section 2.1 describes the use of CPWs as a source of RF current in FMR, and outlines their general characteristics and design, including analytic expressions for the characteristic impedance. Section 2.2 details the design of CPWs for the flip-chip VNA-FMR setup described in Chapter 3, while Section 2.2 discusses the specific design of the lithographically patterned CPWs found in the probe station setup described in Chapter 4.

Next, the specifics of FMR measurement and signal analysis are detailed. Section 2.4 presents Maier-Flaig's technique of derivative divide to produce broadband FMR spectra in the frequency domain. Section 2.5 describes the data collection techniques used in both FMR setups (the flip-chip and microwave probe setups), while Section 2.6 discusses fitting techniques, error handling, and parameter extraction.

2.1 Coplanar waveguide fundamentals

As described in Section 1.2, the tickle field $\boldsymbol{h}_{rf}$ that is used to excite the resonant precession of the magnetization may be produced by an RF current i_{rf}. In this thesis the RF current was generated with a VNA and carried through a coplanar waveguide (CPW). The CPW may be rotated with respect to the external magnetic field to conduct in-plane (IP) or out-of-plane (OOP) FMR, as shown in Fig. 2.1.

CPWs are used for their superior performance over microstrip lines at high frequencies. The coplanar waveguide consists of a center conductor of width w_s which carries the RF signal and two ground planes separated by an air gap of width w_{sg}. The center conductor thus carries the RF current which produces an Oersted field surrounding the conductor

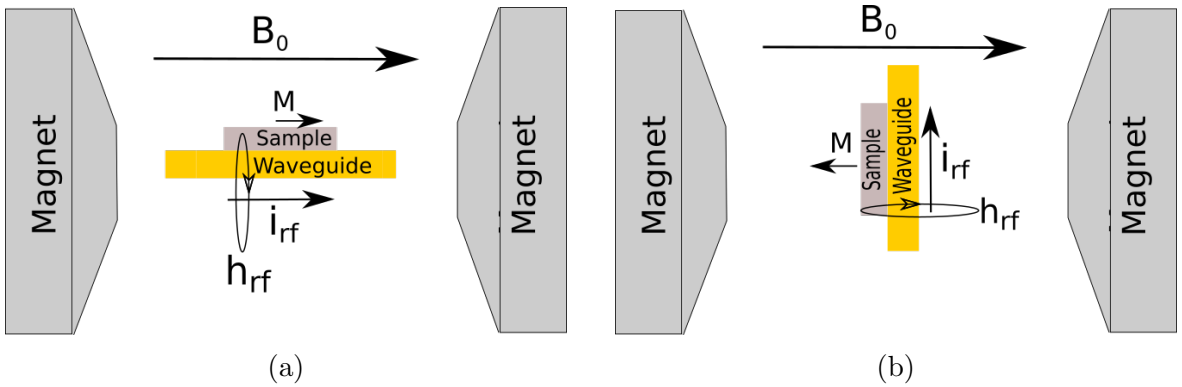

(a) (b)

Figure 2.1: Excitation of FMR with waveguides carrying an RF current i_{rf}, which produces a magnetic tickle field h_{rf} through the Oersted effect. The samples are shown here in the flip-chip orientation with the magnetic sample on top of the waveguide. **(a)** IP FMR, with the magnetization parallel to the thin film and the applied magnetic field. **(b)** OOP FMR, with the magnetization perpendicular to the film and the applied magnetic field.

in the clockwise direction, as seen in Fig. 2.2. CPWs can function with or without a ground backing below the dielectric. The ground backing tends to lower the characteristic impedance. These grounded CPWs (GCPW) usually have metal vias connecting the top ground planes surrounding the center conductor to the bottom ground plane, to prevent the formation of additional modes [21] [22].

The impedance of the VNA and connectors used in the FMR setup are a standard 50 Ω. To avoid unwanted reflections and improve transmission, it is key to design the CPWs to have the same impedance of 50 Ω. Impedance mismatch reflects power and causes amplitude

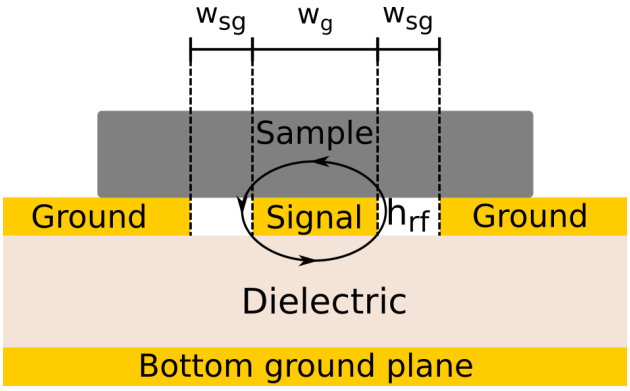

Figure 2.2: Illustration of the flip-chip orientation of a magnetic sample, shown in gray, placed face-down on a coplanar waveguide, shown in gold. The width of the center conductor is given by w_s, and the gap between the center conductor and ground plane is given by w_{sg}, with the thickness of the insulator underneath the top plane as h. A ground plane is shown under the insulator.

ripple at high frequencies, degrading the quality of the FMR signal and reducing the overall sensitivity of the measurement. Therefore, it is essential to calculate the characteristic impedance of a CPW design and bring it as close to 50 Ω as possible over the widest possible frequency band.

A coplanar waveguide, due to the difference in dielectric constant between the air above the conductor and the dielectric below it, cannot support pure TEM modes but rather quasi-TEM modes[23]. The quasi-TEM parameters can be determined analytically by modeling the air-dielectric interfaces as magnetic walls to avoid the effects of fringing fields. To determine its characteristic impedance Z_0, the waveguide is divided into a half-plane, and the capacitance per unit length is computed as the sum of the capacitance of the lower, dielectric-filled region C_{diel} and the capacitance of the upper air-filled region C_{air}[24]. The capacitance is obtained by means of a conformal mapping to convert the CPW geometry into a parallel plate capacitor. The metal is assumed to be infinitely thin and lossless. To derive a simpler analytical expression, the ground planes are assumed to be infinitely large. This is a good assumption for the CPWs described in this report, as the ground plane width is in all cases at least an order of magnitude larger than w_s.

Through this half-plane treatment, the following parameters are used to describe the capacitance per unit length of the line:

$$k = \frac{w_s}{w_s + 2w_{sg}} \tag{2.1a}$$

$$k_1 = \frac{tanh(\frac{\pi w_s}{4h})}{tanh(\frac{\pi(w_s+2w_{sg})}{4h})} \tag{2.1b}$$

$$k_2 = \frac{sinh(\frac{\pi w_s}{4h})}{sinh(\frac{\pi(w_s+2w_{sg})}{4h})} \tag{2.1c}$$

For a CPW with no bottom ground plane, Ghione and Naldi[24] multiply the permittivity by a filling factor, and derive the effective permittivity ϵ_{eff} to be

$$\epsilon_{eff1} = 1 + (\epsilon_r - 1)\frac{\frac{K(k_2)}{K(k_2')}}{\frac{K(k)}{K(k')} + \frac{K(k_1)}{K(k_1')}} \tag{2.2}$$

where ϵ_r is the permittivity of the dielectric layer, and the functions $K(k)$ and $K(k') = K(\sqrt{1-k^2})$ are the complete elliptic integrals of the first kind and its complement, respectively. For a CPW with a bottom conductor, Wadell[25] gives ϵ_{eff} as

$$\epsilon_{eff2} = \frac{1 + \epsilon_r \frac{K(k')}{K(k)}\frac{K(k_1')}{K(k_1)}}{1 + \frac{K(k')}{K(k)}\frac{K(k_1')}{K(k_1)}} \tag{2.3}$$

Finally, the characteristic impedance for the CPW, both with and without a bottom ground plane, is given by

$$Z_0 = \frac{60\pi}{\sqrt{\epsilon_{eff}}} \frac{1}{\frac{K(k')}{K(k)} + \frac{K(k'_1)}{K(k_1)}} \tag{2.4}$$

These techniques for CPW design necessarily make certain simplifying assumptions regarding the geometry of the waveguide. Ghione and Naldi note that the quasi-TEM approximation may not hold for substrate thicknesses beyond $h = 300$ μm. As seen in the next section, the CPWs used for flip-chip have high-frequency dielectric of thickness $h = 762$ μm. This is one possible source of error in calculating the characteristic impedance of the CPWs.

2.2 Flip-chip CPW design

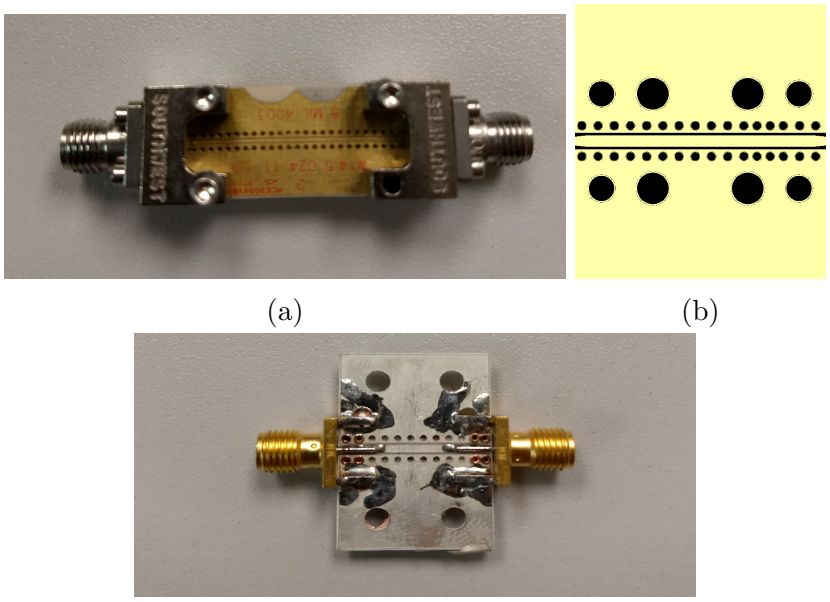

Figure 2.3: **(a)** CPW from Southwest Microwave with end launch connectors, used as starting design for milled waveguides. This CPW uses a thinner dielectric than the milled ones. **(b)** PCB layout of a waveguide, showing mounting holes and vias for grounding the bottom conductor plane. **(c)** The final milled version of the CPW in (b), with soldered connectors and using a silver-plated dielectric. This CPW uses a thicker dielectric substrate than the Southwest Microwave CPW in (a) for reliability reasons.

For the flip-chip FMR setup, the waveguide layout was based on CPWs designed by Southwest Microwave for use with their end launch connectors[26], as seen in Fig. 2.3a. The waveguides had a center conductor width of $w_s = 1.143$ mm (45 mils), and a gap width of $w_{sg} = 254$ μm (10 mils). The waveguides were fabricated with an Othermill PCB

Milling Machine, which milled the PCB design shown in Fig. 2.3b onto a copper-plated Rogers RO4350 dielectric substrate, with a dielectric constant of $\epsilon_r = 3.48$ and a thickness of $h = 0.762$ mm. The substrate was clad in 1 oz per square foot of copper on either side, for a metal thickness of $t = 35.56$ μm (1.4 mils). The board was plated in a layer of 10 microns of silver to reduce oxidation on the copper surface, which can be seen in the final milled waveguide shown in Fig. 2.3c. This helps when soldering end connectors onto the board, and is particularly important when attempting to wirebond to the waveguides, as the wires have trouble bonding to oxidized copper, and have reduced performance even if successfully bonded.

Checking the impedance of this design from Southwest Microwave with Eq. 2.4 and using the effective permittivity of a CPW with a backed ground plane found in Eq. 2.3, the characteristic impedance is found to be $Z_0 = 52.2\ \Omega$. This is fairly close to the desired impedance of 50 Ω, and shows that the Southwest design is a good starting point for designing a milled waveguide for this specific dielectric.

To supplement this analytical design, the LineCalc tool in Agilent ADS[1] was used to check the dimensions of the designed waveguides. This tool does not make the infinite ground plane assumption, and also takes in the finite thickness of the metal conductor. With the given dimensions, the impedance was found to be $Z_0 = 49.66\ \Omega$. This more accurate estimate of Z_0 gives confidence in the CPW design using these basic dimensions.

The CPW design includes tapering in the transmission line by the connectors so that the line can compensate for the excess capacitance caused by the presence of the connector pin sitting on the top of the center conductor. Narrowing the trace in a taper thus increases the board's inductance to keep the line matched at 50 Ω. The line was thus linearly tapered from its default dimensions to end dimensions of $w_s' = 889$ μm (35 mils) and $w_{sg}' = 381$ μm (15 mils). This taper was simulated in Southwest Microwave's design, and was shown to compensate for the connector pin capacitance and keep the characteristic impedance close to 50 Ω.

2.3 Lithographically patterned waveguide design

As described in Chapter 4, CPWs with much smaller dimensions were fabricated with photolithography and deposited directly on top of the magnetic layer. These were designed to have better coupling to the ferromagnet than would be possible in the flip-chip setup, and to be accessible with microwave probe tips rather than soldered connectors. The design of these patterned waveguides is thus different from that of the aforementioned milled waveguides.

The substrate consisted of 500 μm of diced Si wafer, with 250 nm of thermally grown oxide on top. Because the Si is so much thicker than the SiO_2, the oxide is ignored in the CPW analysis and the dielectric constant is taken to be the value for Si, $\epsilon_r = 11.7$. The substrate thickness is thus $h = 500$ μm. The waveguide consist of 150 nm of thermally evaporated Au, as described in Chapter 4. The magnetic layer is assumed to be coupled

[1] Keysight Technologies

to the waveguide, so that the total conductor consists of the waveguide together with the conducting magnet. The effective metal thickness t can thus vary depending on the magnetic layer thickness, but here the simplest case is taken, with $t = 150$ nm. The lithographically patterned waveguides differ from the milled ones in the previous section in that they do not possess a ground backing on the bottom.

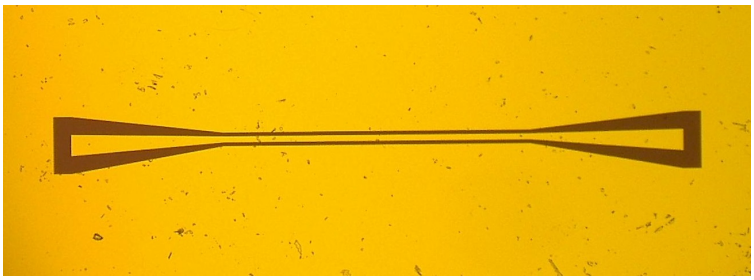

Figure 2.4: Microscope image of lithographically patterned CPW, showing RF pads for microwave probes at either end and tapering to default CPW dimensions of $w_s = 20$ μm and $w_{sg} = 12$ μm.

Based off designs for previous CPWs used for spin transport measurements in literature [27] [28], the center conductor width is chosen to be in the range of 30 μm. Using Eq. 2.2 for the permittivity of a CPW without a ground plane, with the previously listed parameters for the substrate and conductor, the dimensions initially chosen were $w_s = 30$ μm and $w_{sg} = 10$ μm. However, from Eq. 2.4, Z_0 is found to be 43.2 Ω for this case. The CPW dimensions were thus modified until reaching values of $w_s = 20$ μm and $w_{sg} = 12$ μm. In this case the impedance is calculated analytically as $Z_0 = 52.2$ Ω. The LineCalc tool, however, finds Z_0 to be 49.93 Ω. Eq. 2.4 is unaffected by line length, so L was chosen to be 1000 μm by default. These were the final dimensions chosen for the lithographically patterned CPWs.

However, although these small dimensions are adequate for the main line, the CPW must have larger landing pads for use with microwave probes. Similarly to the milled waveguides, the line is thus linearly tapered from its default dimensions, but in this case the line is tapered outward to become larger, rather than inward to become smaller. The CPW is thus linearly tapered from $w_s = 20$ μm and $w_{sg} = 12$ μm to maximum tapered dimensions of $w_s^{'} = 100$ μm and $w_{sg}^{'} = 58$ μm. These tapered dimensions can be calculated to have an impedance of $Z_0 = 51.63$ Ω, similar to that of the default line. Indeed, since Eq. 2.4 only depends on the ratio of w_s and w_{sg}, the absolute dimensions of a CPW may be changed while keeping the same characteristic impedance Z_0 as long as $\frac{w_s}{w_{sg}}$ is kept the same [29]. An example of a finished CPW with tapered landing pads can be seen in Fig. 2.4.

2.4 VNA-FMR signal analysis in the frequency domain

As mentioned in Section 1.2, at the resonant condition the absorption takes the form of a complex Lorentzian with a center frequency of $\omega_{res}(B_0)$ (related to the external magnetic field B_0 by Eq. 1.9) and a full-width half-maximum of $\Delta\omega$, as described in Section 1.2. The absorption is given by the susceptibility χ, which takes the form

$$\chi(\omega, B_0) = \frac{\omega_m(\gamma B_0 - i\Delta\omega)}{[\omega_{res}(B_0)]^2 - \omega^2 - i\omega\Delta\omega} \tag{2.5}$$

This complex Lorentzian is fit to the frequency-swept data from the VNA. The total system consisting of the CPW connected to the VNA is a two-port RF device with voltage V_1 at port 1 and V_2 at port 2, producing a 2x2 scattering matrix. The transmission coefficient is $S_{21} = \frac{V_2}{V_1}$, a complex ratio indicating the insertion loss through the CPW. The change in RF current absorption due to resonance is reflected as a change in S_{21}.

However, rather than fit the change in S_{21} to the susceptibility χ, in this thesis a method known as derivative divide, described by Maier-Flaig[30], is used to numerically calculate the derivative of S_{21}. The derivative divide method relates the voltage induced in the center conductor of the CPW to χ as

$$V_{inductive} = -i\omega A e^{i\phi} V_2 \chi(\omega, B_0) \tag{2.6}$$

where A is a real-valued proportionality constant and $e^{i\phi}$ is a phase factor due to the electrical length of the microwave leads and the CPW. V_2, the voltage at port 2, is then separated from the frequency-dependent background signal $V_{2,background}(\omega)$ to parameterize the S_{21} signal as

$$S_{21} = \frac{-i\omega A V_2 \chi(\omega, B_0) + V_{2,background}(\omega)}{V_1} e^{i\phi} \tag{2.7}$$

The difference of S_{21} with respect to B_0 using a finite field step width ΔB_{mod} is calculated as the $d_D S_{21}$ signal:

$$\begin{aligned} d_D S_{21} &= \frac{S_{21}(\omega, B_0 + \Delta B_{mod}) - S_{21}(\omega, B_0 - \Delta B_{mod})}{S_{21}(\omega, B_0)\Delta B_{mod}} \\ &= -i\omega A \frac{\chi(\omega, B_0 + \Delta B_{mod}) - \chi(\omega, B_0 - \Delta B_{mod})}{\Delta B_{mod}} \end{aligned} \tag{2.8}$$

The derivative divide method was developed to produce a frequency-swept, broadband FMR signal, and has been shown to yield equivalent results compared to the usual method of directly analyzing the change in S_{21}. The component $V_{2,background}$ drops out in the $d_D S_{21}$ signal, so that background noise and non-magnetic field dependent features are suppressed.

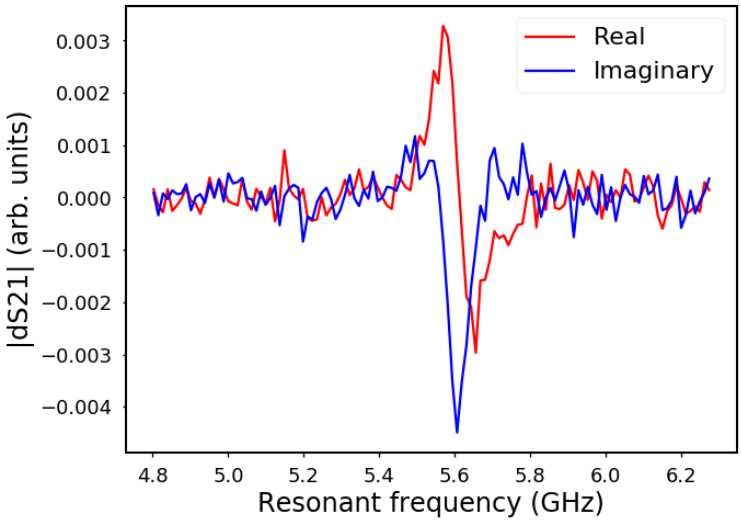

Figure 2.5: A representative frequency sweep at a fixed magnetic field, showing the FMR signal calculated from the S_{21} using the dS21 technique in Eq. 2.8.

Furthermore, because it relies only on the changes in S_{21}, it also functions without the need for VNA calibration. The $d_D S_{21}$ signal produces a complex Lorentzian, as shown in Fig. 2.5, that can be fitted to Eq. 2.5 and determine ω_{res} and $\Delta\omega$, from which the desired FMR parameters can be fitted.

2.5 Data measurement and collection

A vector network analyzer (VNA) is a high-frequency measurement device used to characterize RF devices by measuring the scattering parameters of up to four RF ports. An HP 8722D VNA, shown in Fig. 2.6, was used to provide the RF current for the tickle field h_{rf}, and to measure the change in absorption in order to characterize the FMR signal.

A LabVIEW[2] software system was used to control the magnetic field controller, control the VNA sweep parameters and store the measured S21 data, and display the dS21 sweep results. The LabVIEW scripts store the raw S_{21} data and operate the VNA, magnetic field controller, and other instrumentation needed for the FMR sweep. The data is then analyzed with Python scripts to perform the fitting. The derivative divide of the S_{21} data is calculated for each magnetic field sweep, and then the frequency data is windowed and fit to the Lorentzian function χ.

The LabVIEW scripts allowed control over the field step size and magnetic field and frequency sweep limits. It could also modify VNA parameters such as the input power level, IF bandwidth, number of sweep points, and number of averaging measurements (if

[2]National Instruments Corporation

Figure 2.6: An HP 8722D VNA used for FMR measurements. The 8722D has a frequency range of 50 MHz to 40 GHz, and can output signals with a power of -5 dBm up to 20 GHz, or -10 dBm up to 40 GHz. The SMA connectors used in this setup limit the maximum frequency to 25 GHz, however.

necessary). The field step size, number of points, IF bandwidth, and number of averaging measurements all affect the sensitivity, SNR, and scan time of a given sweep [31].

The IF bandwidth refers to the intermediate frequency filter used to downconvert from the RF signal to baseband. Modern equipment use multiple intermediate mixer and filter stages to downconvert from RF to baseband, as seen in Fig. 2.7a, with the final IF filter having an adjustable bandwidth. A narrower IF bandwidth tends to reject noise in the sidebands surrounding a signal (Fig. 2.7b), and thus increases SNR at the cost of higher measurement time due to the need for additional spectrum acquisitions.

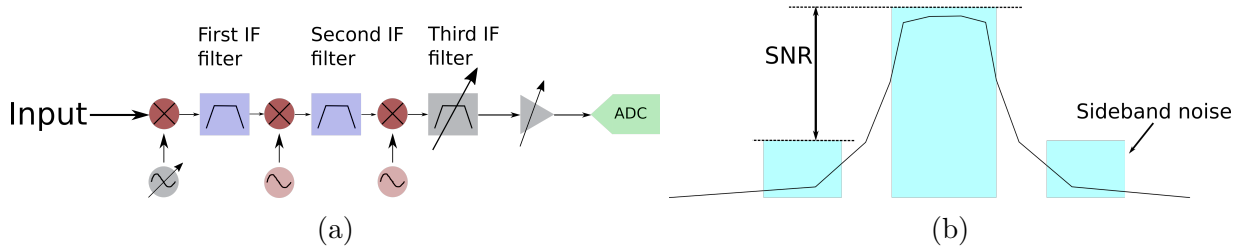

Figure 2.7: **(a)** A schematic of the downconversion process in a spectrum analyzer, showing multiple stages of mixers and filters. **(b)** An IF bandwidth applied over a signal in the frequency domain, with noise power located in the sidebands.

The effect of lowering the IF bandwidth can be dramatic, as seen in Fig. 2.8. For a 30 nm Py sample, lowering the IF bandwidth from 100 to 30 Hz increased the SNR by approximately a factor of 2. As this project was mostly concerned with the construction and validation of FMR setups, an IF bandwidth of 100 Hz was used by default in the sweeps to allow for fast data collection. However, to obtain the most sensitive possible signal, the

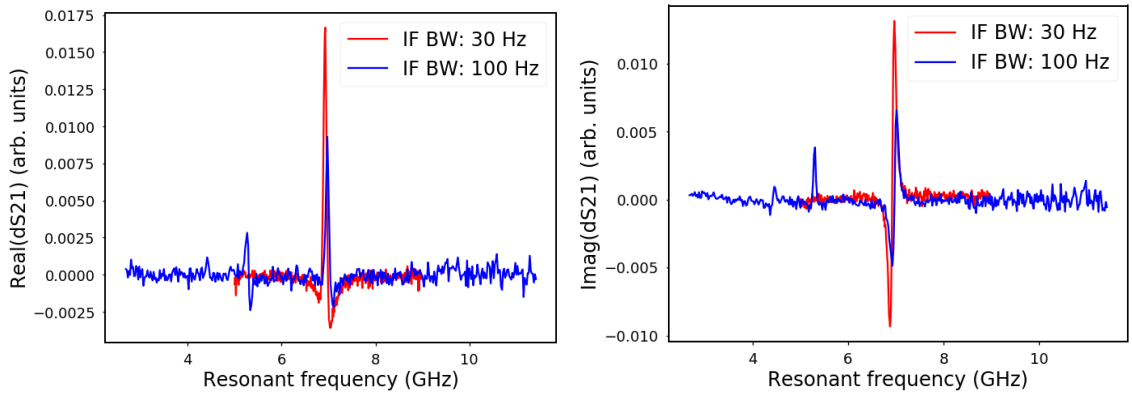

(a) (b)

Figure 2.8: FMR signal for a 30 nm Py film at fixed magnetic bias as a function of frequency, showing **(a)** the real and **(b)** imaginary part of the signal. The blue line indicates a measurement with the standard IF bandwidth of 100 Hz. The red line shows a measurement with the IF bandwidth lowered to 30 Hz. The minimum IF bandwidth is 10 Hz.

smallest possible IF bandwidth should be used in VNA-FMR. This is especially crucial when measuring weak FMR signals from very thin films or materials with low magnetizations.

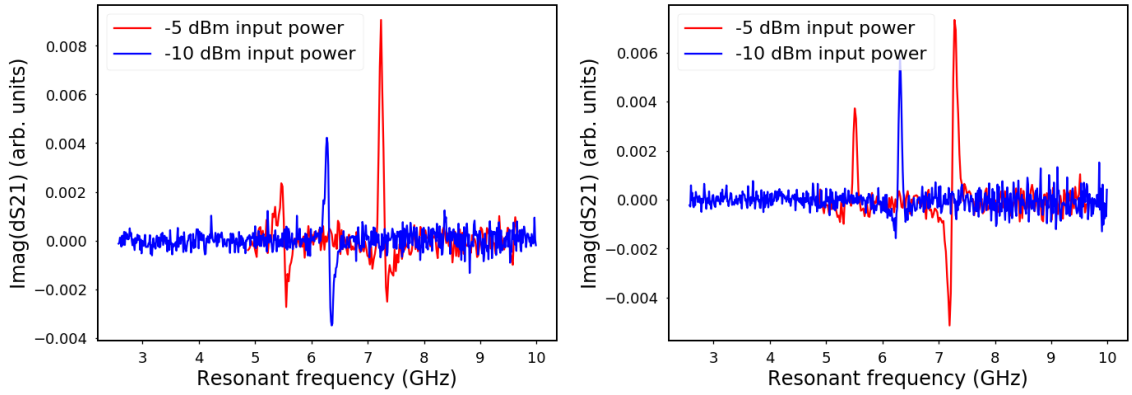

(a) (b)

Figure 2.9: FMR signal for a 30 nm Py film at fixed magnetic bias as a function of frequency, showing **(a)** the real and **(b)** the imaginary part of the signal. The red line shows a measurement with the power level from the VNA set to -5 dBm; the VNA power level was -10 dBm for the blue line. A second mode is visible in the measurement at -5 dBm, shown as a second resonance peak.

The default input power level used in the FMR sweeps shown in this thesis was -10 dBm. However, the HP 8722D VNA can output up to -5 dBm in source power, more than three

times the power supplied by -10 dBm. As seen in Fig. 2.9, this increase in source power can cause a modest but noticeable increase in FMR signal.

2.6 Fitting techniques

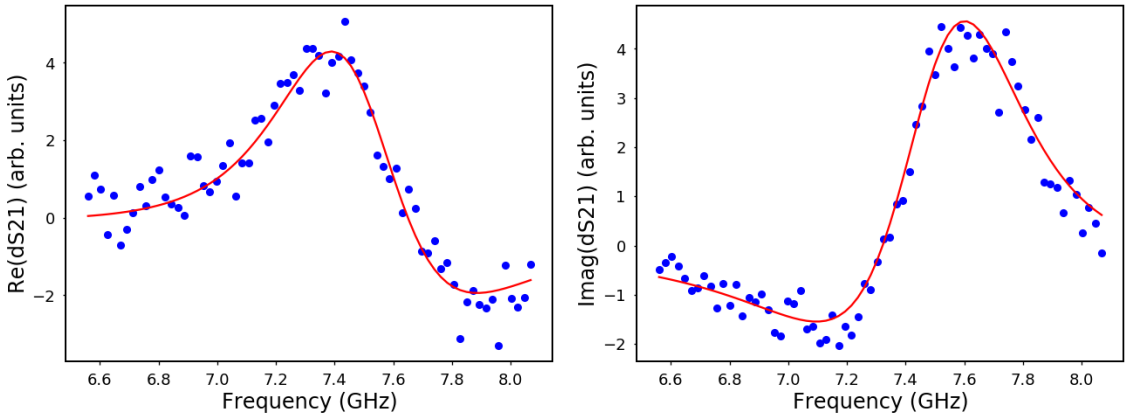

(a) (b)

Figure 2.10: A representative portion of an FMR measurement vs frequency at fixed magnetic field, showing the **(a)** real and **(b)** imaginary portions of the dS21 signal. The blue dots indicate the dS21 data points calculated from the data stored by the VNA using Eq. 2.8. The red line is a fit to the complex Lorentzian function given in Eq. 2.5. The center frequency of the Lorentzian is found by windowing the signal around the peak dS21 value.

Fitting is done using the LMFit library in Python, which uses the Levenburg-Marquardt method of non-linear optimization for curve fitting. The algorithm uses peak finding to fit the signal: it searches for the highest amplitude point over a given frequency range, then takes that point to be the peak of the Lorentzian, an example of which is shown in Fig. 2.10. The frequency range is windowed by restricting the searchable frequency range to an area centered around the average resonant frequency of the 6 previous resonant frequencies fitted by the algorithm. Thus, the algorithm starts out by naively finding the peak amplitude and fitting to those values, and after six iterations begins windowing the frequency range to more accurately peak search. However, if background noise is high, the peak amplitude due to resonance is low, or if there are spurious features with higher amplitudes than the resonance peak, the algorithm will incorrectly identify the location of the peak in frequency. The algorithm will then attempt to fit the spurious feature or background noise to the Lorentzian function χ, with a higher degree of error than usual (as indicated by a higher chi-squared error function).

The plots of resonance frequency vs magnetic field displayed in this thesis usually limit the peaks to fits with a χ^2 error less than 200, to filter out these spurious fits. Nevertheless,

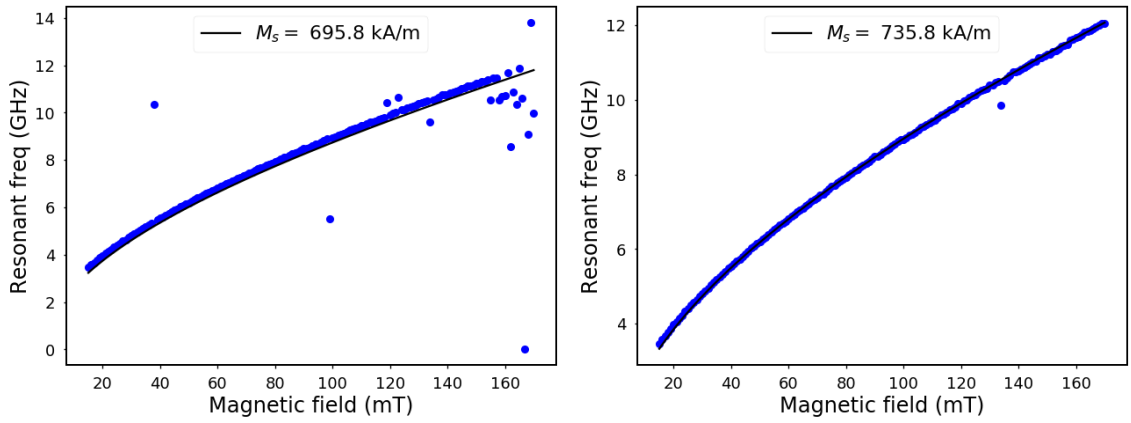

(a) (b)

Figure 2.11: **(a)** An in-plane FMR sweep of resonant frequency f_{res} vs magnetic field on a 10 nm Py sample, after fitting each field slice to a Lorentzian and fitting the f_{res} to Eq. 1.7a. The blue dots scattered about the resonant frequency curve indicate points where the automatic fitting failed to locate the proper peak, and fit to the wrong frequency window. **(b)** The same FMR sweep, run through an iterative fit which windows the frequency range based on the resonant frequency curve extracted in (a).

spurious fits and errors in peak finding are a serious problems in even moderately noisy data, or in samples with a low magnetization–and thus a low peak amplitude at resonance. In Fig. 2.11a, for a thin 10 nm Py sample the signal is relatively weak, and sometimes swamped out by background noise, causing errors in peak finding and extracting an incorrect $\boldsymbol{M_s}$.

To improve peak finding, after running an initial fit iteration across the entire magnetic field range and fitting the overall resonant frequency curve to the Kittel formula, the algorithm uses the resonant frequencies predicted by the fitted Kittel equation to window the frequency range and rerun the fitting. This iterative fitting improves peak finding by more effectively windowing the frequency range to search for the peak. With a good initial fit to the Kittel equation, the iterative fit can better locate peaks and fit the frequency at a given magnetic field value. As seen in Fig. 2.11b, for a 10 nm Py sample the iterative fit corrected the majority of the fitting errors and changed the value of the extracted $\boldsymbol{M_s}$ by almost 6%. However, this technique only improves the windowing of the frequency range to find the peak, and still relies on finding the peak amplitude to find the resonant peak. Furthermore, it requires a reasonable initial fit to the Kittel equation to window the resonant frequencies properly. Thus, for a weak signal which is swamped by background noise or other, spurious features, this approach has limitations.

The in-plane frequency linewidth curve tends to show a large amount of variance around the fitted curve described by Eq. 1.14. As a result, the fit to this curve, and thus the extracted value of alpha, is highly influenced by the fit area. This is especially true when fitting at lower frequencies, as the large linewidths seen can greatly affect the fitted curve.

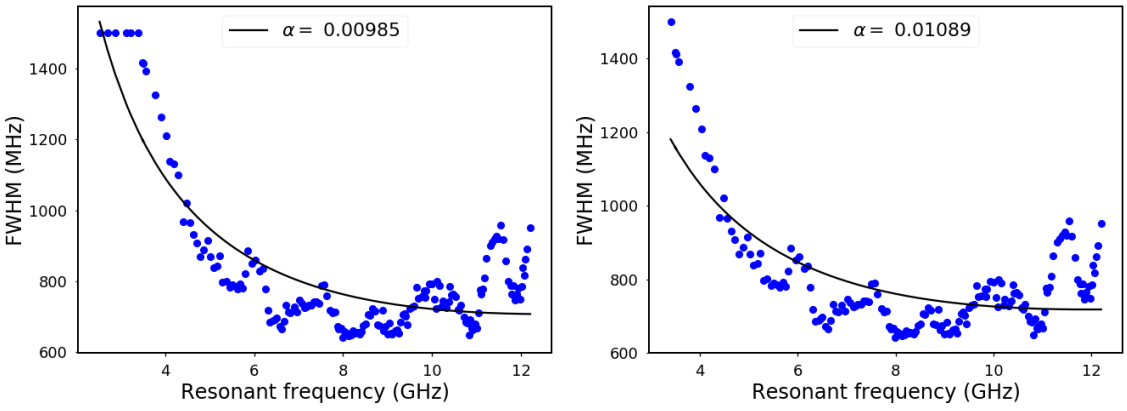

(a) (b)

Figure 2.12: Frequency linewidths Δf as a function of resonant frequency f_{res}, extracted from an in-plane FMR sweep of an 80 nm Py sample and fit to Eq. 1.14. The FWHM for a given field value are shown as a blue dot, while the black line indicates the overall curve fit. **(a)** The FWHM curve fit from 10 mT to 160 mT. **(b)** The same FMR spectrum, with the FWHM curve fit from 15 mT to 160 mT. With lower field sweep values excluded, lower frequency parts of the curve are excluded as well.

As an example, in Fig. 2.12, changing the fit area by just 5 mT (starting the fit at 10 mT, as in Fig. 2.12a rather than 15 mT, as in Fig. 2.12b)changes the extracted value of alpha by 10%. In general, to obtain the most robust value of α, the linewidth curve should be fit over the largest possible frequency and field range or averaged over many measurements[32], although this requires a longer sweep time.

Chapter 3

Flip-chip FMR setup and measurement of permalloy thin films

This chapter presents the the design and validation of a flip-chip VNA-FMR setup, in which magnetic samples are placed on a larger CPW and the change in absorption through the CPW is measured. This is a typical geometry for FMR setups, as it allows for quick and easy measurements of a wide variety of ferromagnetic films. While most FMR setups are constrained to measure FMR in either the in-plane (IP) or out-of-plane (OOP) orientation, the FMR setup presented here can conduct both kinds of measurements. This gives it greater flexibility to measure samples with IP or OOP magnetization.

In the first part of the chapter, the experimental setup is detailed, along with its ability to make IP and OOP measurements. Section 3.2 discusses some of the considerations taken into account when conducting flip-chip FMR, such as the change in CPW transmission caused by the sample's presence, as well as its effect on overall signal strength.

Next, the setup is validated by conducting measurements on permalloy ($Fe_{20}Ni_{80}$) thin film samples. Permalloy (Py) is a well-studied ferromagnetic alloy, making it easy to compare measurement results to those found in literature. It also has a large IP magnetization that produces an FMR signal of relatively high magnitude, making it easier to fit. Section 3.3 details the fabrication of a Py thickness series (10, 18, 30, 80 nm) on a high-resistivity Si substrate. In Section 3.4, the results of FMR sweeps on the thickness series are presented for the IP orientation. The fitted magnetization and damping are discussed as a function of thickness. In Section 3.5, the samples are biased along their hard axis in the OOP direction, and a transition from IP to OOP resonance is observed in the subsequent FMR sweeps. Finally, the effect of different substrates on the OOP FMR characteristics is also studied, and found to greatly affect the damping.

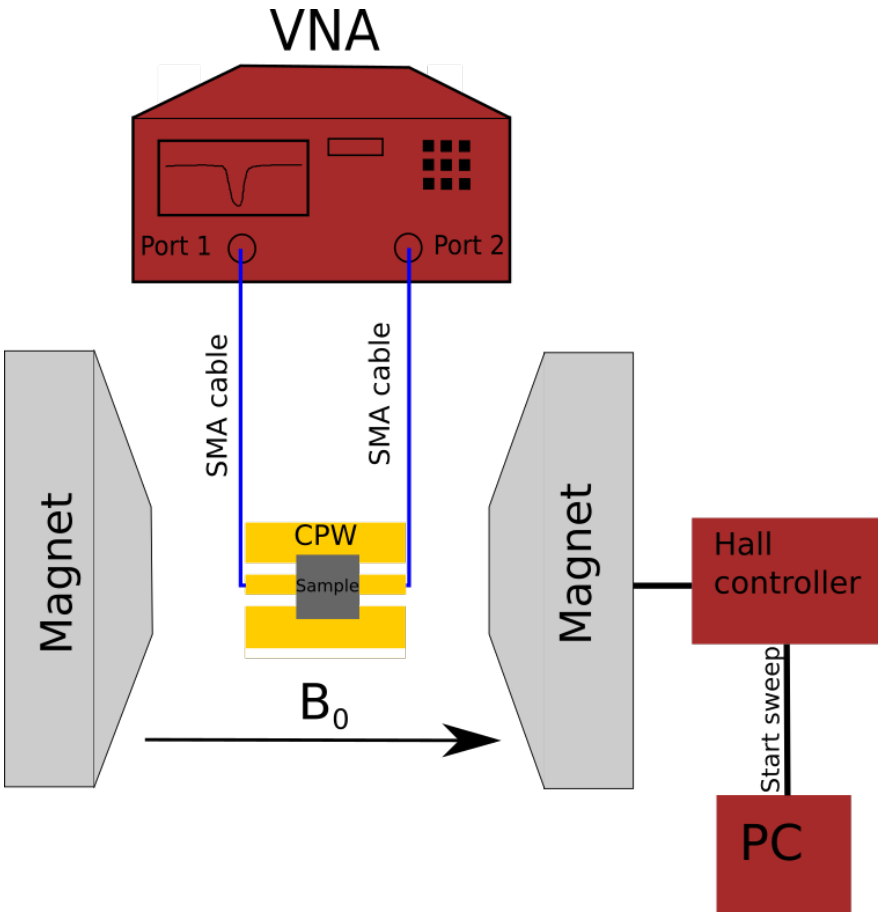

Figure 3.1: A schematic illustration of the overall flip-chip FMR setup.

3.1 Experimental setup

A diagram of the overall flip-chip setup is shown in Fig. 3.1. A magnetic sample was placed face-down (substrate up) on a CPW, and placed between the pole pieces of a Bruker ER 073 magnet. The magnet can supply DC fields up to 1 T, and provides excellent field uniformity between the pole pieces. The magnet is controlled by a Bruker ER 032M field controller, which uses a Hall effect sensor to determine the DC magnetic field. The CPW is connected to the VNA with SMA cables. The VNA and field controller are both connected to a computer which contains the LabVIEW scripts to run the FMR sweeps and collect the data, as described in Section 2.5.

An aluminum sample holder was designed in CAD and fabricated in a machine shop, consisting of a plate to hold the apparatus on a table above the magnet, a hollow circular arm routing the SMA cable down to the waveguide between the magnetic pole pieces, and a rectangular bracket to hold the waveguide in place. The arm was placed on a circular bracket to allow rotation for angular dependence measurements, and to allow samples to easily be

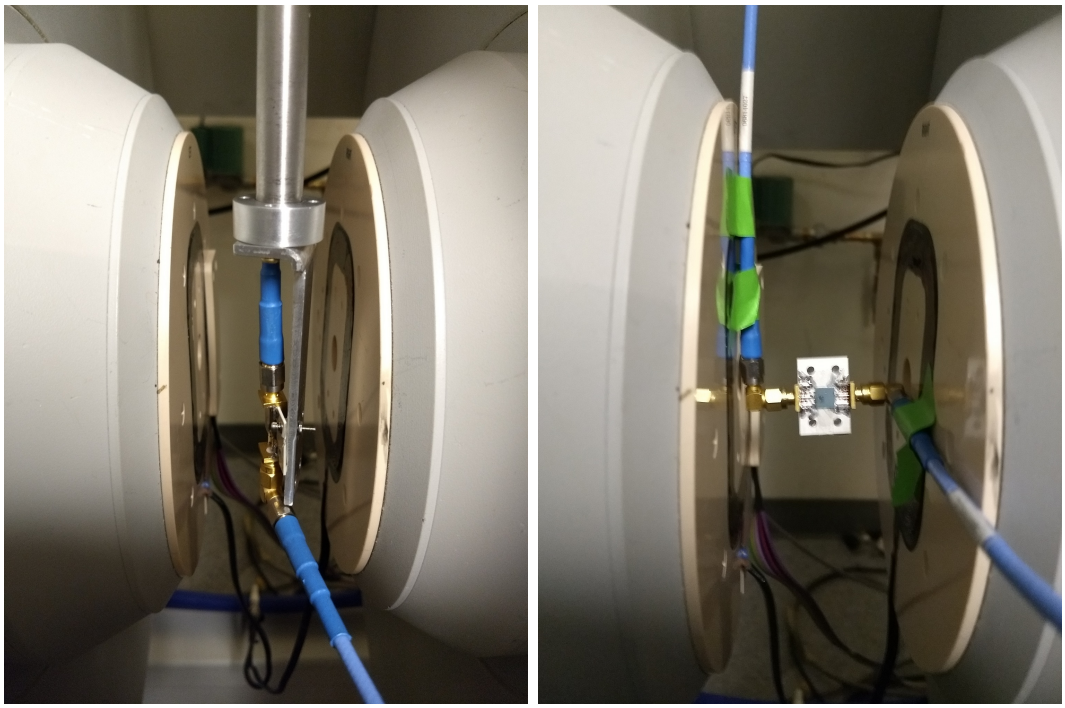

(a) (b)

Figure 3.2: The flip-chip FMR setup, with the CPW attached to the sample holder and the sample placed on the CPW center conductor. **(a)** The sample holder rotates the sample perpendicular to the magnetic field for an out-of-plane measurement. **(b)** The sample is rotated parallel to the magnetic field for an in-plane measurement, and the waveguide is rotated 90 ˚so the RF current is parallel to the field lines between the pole pieces.

measured in an IP or OOP orientation. To measure samples in the OOP configuration, the sample holder was rotated so that the waveguide was pointed perpendicular to the magnetic field, with the waveguide's center conductor facing directly down (Fig. 3.2a. However, to measure samples in the IP configuration the waveguide center conductor had to be parallel to the magnetic field, with the waveguide positioned horizontally rather than vertically. The magnetic pole pieces have a horizontal spacing of 2.5 inches, so a special, short waveguide was developed to fit between the pole pieces with enough space for angled SMA connectors.

Care was taken to ensure that no magnetic components were present in the setup, which necessitated the purchase of nonmagnetic connectors and cabling. The SMA cabling was measured and rated up to the connector limit of 25 GHz. The waveguide was secured to the sample holder with bolts, and for a given measurement the sample was placed face down on top of the waveguide in the "flip-chip" method and secured with sticky vacuum grease to prevent it from falling.

While many ferromagnetic resonance experiments provide isolation between the sample and the waveguide, using a thin insulating layer such as double-sided tape, it was found that

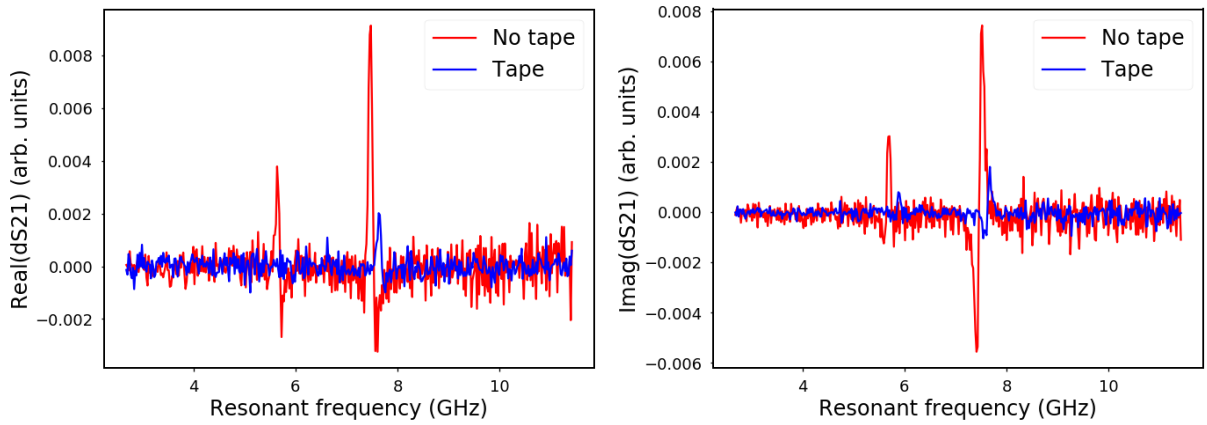

(a) (b)

Figure 3.3: FMR signal of a 30 nm Py film at fixed magnetic bias as a function of frequency, showing the **(a)** real and **(b)** imaginary portions of the signal. The red line shows the signal with the sample placed directly face-down on the CPW with no isolation; the blue line shows the result of placing double-sided tape between the CPW and the sample.

an isolation layer significantly lowered the strength of the FMR signal, as shown in Fig. 3.3. Any reduction in coupling between the CPW and magnet has a strong effect on the signal strength. Tape is especially unsuitable as an isolation layer because bumps or creases in the tape can separate the magnetic film from the CPW. For the flip-chip FMR setup, therefore, no isolation layer is used.

3.2 CPW transmission and RF characteristics

As discussed in the previous section, great care is taken to ensure that waveguides have a matched impedance of 50 Ω, to prevent large reflections that limit the setup's sensitivity and to remove amplitude ripple that swamps the dS21 signal. However, in the flip-chip geometry, placing a conducting sample directly on the waveguide's center conductor—touching both the center conductor and ground plane—can change the RF characteristics substantially, and introduces an extra inductance that modifies the characteristic impedance and leads to additional reflections [33].

To measure the effect of a conducting chip on the waveguide's scattering parameters, a waveguide used for OOP FMR measurements (created on the Othermill machine) was measured by a VNA, with S_{11} and S_{21} shown in Fig. 3.4. The presence of any flip-chip sample increases reflection and greatly decreases transmission. S_{21} is slightly lower when using $LiNbO_3$, a piezoelectric, as the substrate compared to Si. Although the S_{21} signal is affected by the presence of a conductive path between signal line and ground, the placement of a sample does not seem to greatly affect the extracted dS21 signal.

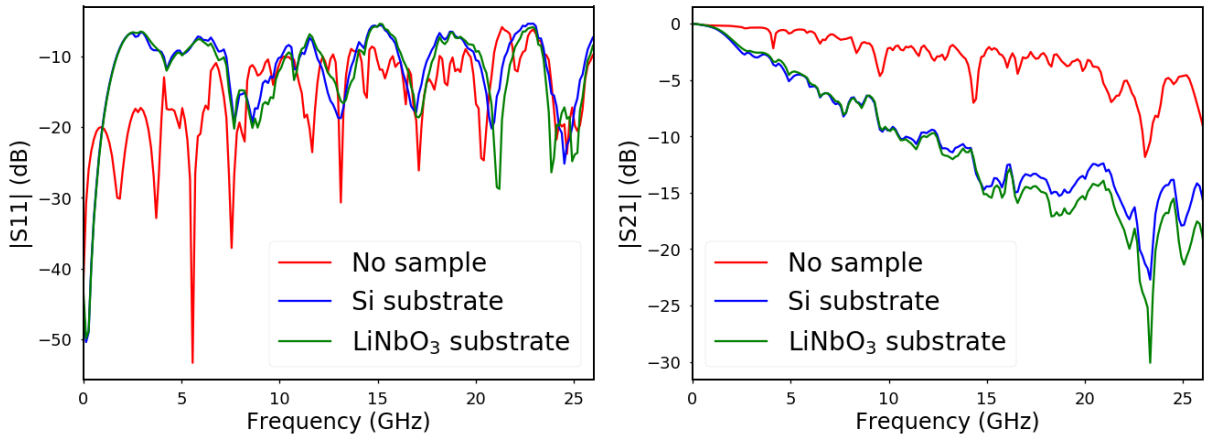

(a) (b)

Figure 3.4: **(a)** The S_{11} of one of the CPWs measured on the VNA. The red line indicates the reflection of the CPW alone, while the blue and green lines indicate the measured reflection with samples grown on high-resistivity Si and $LiNbO_3$ substrates placed on the CPW. **(b)** The measured S_{21} of the CPW.

In an attempt to improve the strength of the resonant peak and increase the SNR, an Agilent 83006A broadband RF amplifier was added to the signal path to provide RF gain. The 83006A supplies 20 dB of gain over the frequency range of 100 MHz to 26.5 GHz, approximately the same range covered by the SMA connectors used in the setup. To avoid saturating the VNA, an attenuator providing 10 dB of attenuation up to 26.5 GHz was added. Together, the amplifier and attenuator added 10 dB of gain over the entire frequency range. An FMR sweep was carried out for a 30 nm Py film on a high-resistivity Si substrate with the amplifier and attenuator attached to the cabling, as shown in Fig. 3.5.

However, because the $d_D S_{21}$ signal is based off the derivative of S_{21}, constant offsets in S_{21} do not affect the strength of the FMR spectrum. Only variation in S_{21} contributes to the SNR. As a result, the amplifier, which adds 20 dB of gain across the entire frequency band, does not improve the FMR signal noticeably. Since the absolute magnitude of S_{21} does not affect the spectrum, it may seem that poor transmission caused by impedance mismatch does not matter, as long as the transmission is above the intrinsic noise of the system. However, impedance mismatch also causes amplitude ripple due to micro-reflections on the line. This amplitude ripple is discussed in more detail in Section 4.2. Nevertheless, the constant S_{21} offset provided by the amplifier (in conjunction with the attenuator) does not improve the SNR.

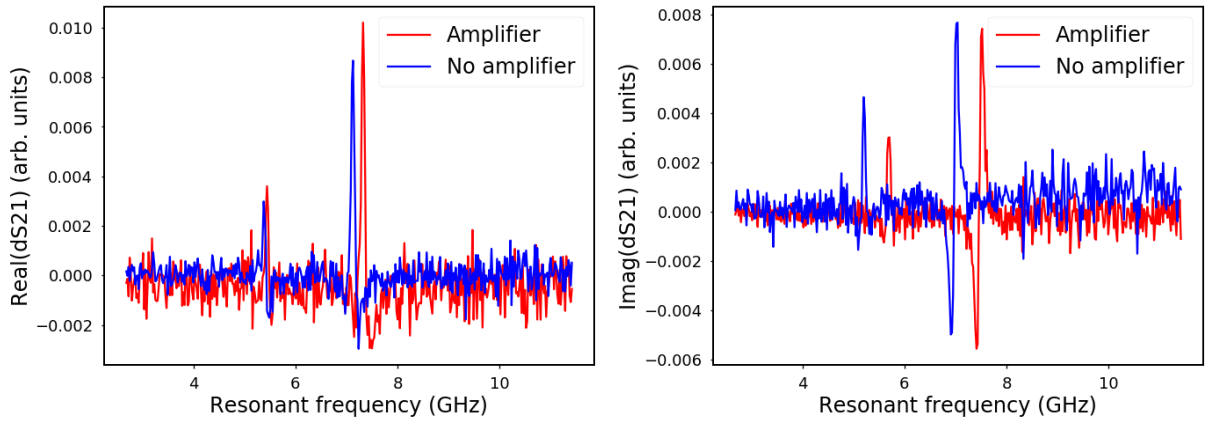

(a) (b)

Figure 3.5: FMR signal of a 30 nm Py film at fixed magnetic bias as a function of frequency, showing the **(a)** real and **(b)** imaginary portions of the signal. The blue line shows the normal signal with no amplifier or attenuator added; the red line shows the FMR signal with a 20 dB amplifier and 10 dB attenuator added, for a total of 10 dB of gain.

3.3 Sample fabrication

To demonstrate the effectiveness of the flip-chip FMR system, measurements were conducted on permalloy thin films in the in-plane and out-of-plane orientations.

The Py films were grown by magnetron sputtering with 30 W of power at an Ar pressure of 2 mTorr, using a deposition rate of 0.196 Å/s. The samples were deposited on substrates made of high-resistivity Si (topped with 250 nm SiO_2), glass, $LiNbO_3$, and quartz, to compare the effects of the substrate at high frequency. Various thicknesses of Py are deposited ($d_x = 10, 18, 30$ and 80 nm), and all samples were capped with 2 nm of MgO to prevent oxidation. No magnetic field was applied during the sample growth, and all samples thus have an in-plane magnetization, as is standard for Py.

The samples all had dimensions of 7.6x7.6 mm except for the quartz chip, which had dimensions of 2.6x2.6 mm. The 80 nm sample (on high-resistivity Si) was measured on a vibrating sample magnetometer (VSM) in both IP and OOP orientations, as seen in Fig. 3.6. The total magnetic moment at saturation was measured as $m = 4.106\ \mu A - m^2$ in-plane and $m = 2.807\ \mu A - m^2$ out-of-plane. Dividing by the volume of the sample, the saturation magnetization is thus $\boldsymbol{M}_S = 888.7$ kA/m when aligned IP and $\boldsymbol{M}_S = 607.4$ kA/m when aligned OOP. The IP value of $\boldsymbol{M}_s$ is typical for Py thin films [34] [35] [5]. Since the sample has an IP magnetization, a substantial OOP field (900 mT) is required to tilt the magnetization OOP and align all the spin in that direction to reach saturation.

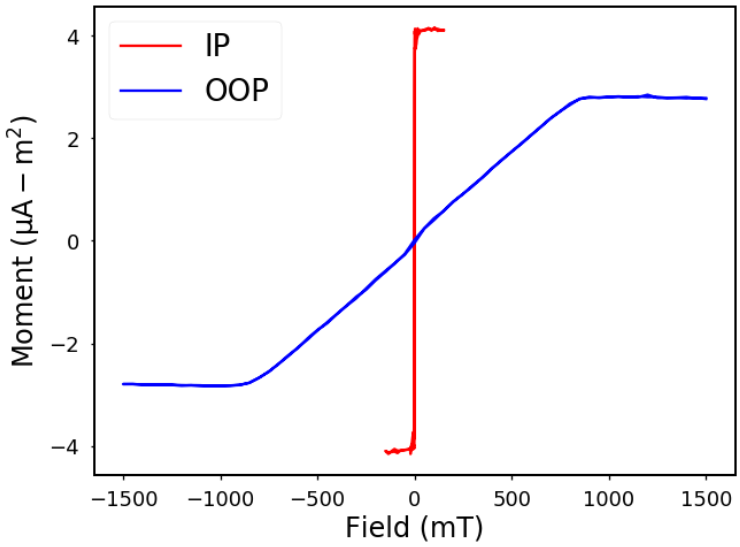

Figure 3.6: A vibrating sample magnetometer (VSM) measurement of the total magnetic moment m vs magnetic field,conducted on MgO(2)/Py(80)/SiO_2(0.25)/Si(substrate) with in-plane magnetization and measured in the in-plane (red) and out-of-plane (blue) orientations.

3.4 FMR in the in-plane orientation

First, the results of IP FMR are presented for the Py thickness series. All the measured films are on the high-resistivity Si, as a result of the lower damping on this substrate (this is discussed in Section 3.5). Because the Py has an IP easy axis, the magnetization saturates at very low fields (Fig. 3.6), and so the magnetic field sweep was run starting at 0 mT. The maximum field value was 200 mT, as above this point high-frequency noise exceeded the FMR signal. As discussed in Section 2.6, the resulting fit is greatly affected by the fit area chosen, and the best fit area was found to be from 15 mT to 160 mT, due to errors in linewidth at very low magnetic fields. In Fig. 3.7, for each film thickness the resonance frequency for a given magnetic field has been found by fitting to a complex Lorentzian, and the resulting resonant frequency vs magnetic field curve has been found from a fit to Eq. 1.10a. The extracted $\boldsymbol{M_s}$ is displayed for each thickness. The value of the gyromagnetic ratio γ and Landé factor g was also found from this fit. g was found to be 2.016, 2.056, 2.039, and 1.98 for the 80, 30, 18, and 10 nm films, respectively (Table 3.1), somewhat lower than the literature value of 2.1-2.14 for Py [5] [36].

Comparing the extracted $\boldsymbol{M_s}$ is displayed for each thickness, as in Fig. 3.9a, it is clear that the magnetization is similar for each film regardless of the thickness, although the 18 nm film has a somewhat smaller magnetization. As this is a material-specific parameter, $\boldsymbol{M_s}$ should be unaffected by the film thickness. The extracted magnetization has an average value of $\boldsymbol{M_s} = 679.8$ kA/m, with an average standard deviation of 0.17% on the fit.

The average $\boldsymbol{M_s}$ differs from the IP value of $\boldsymbol{M_S} = 888.7$ kA/m measured on the VSM for

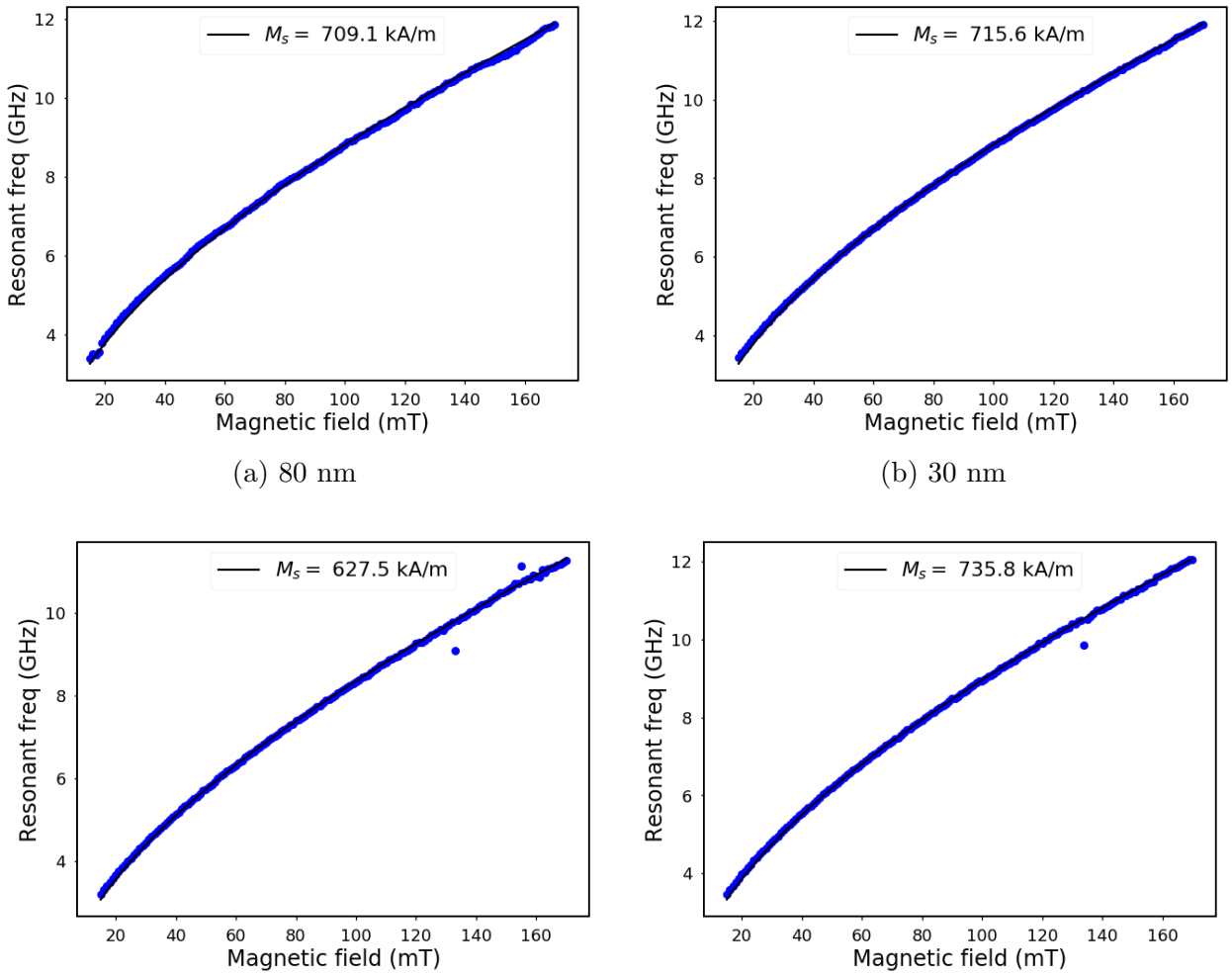

(a) 80 nm

(b) 30 nm

(c) 18 nm

(d) 10 nm

Figure 3.7: Resonance frequency as a function of magnetic field, swept from 15 mT to 160 mT, for the Py(n)/SiO_2(0.25)/Si IP thickness series, for films of thicknesses **(a)** 80, **(b)** 30, **(c)** 18, and **(d)** 10 nm. The fit to Eq. 1.10a is plotted in black, and the extracted $\boldsymbol{M_s}$ is displayed.

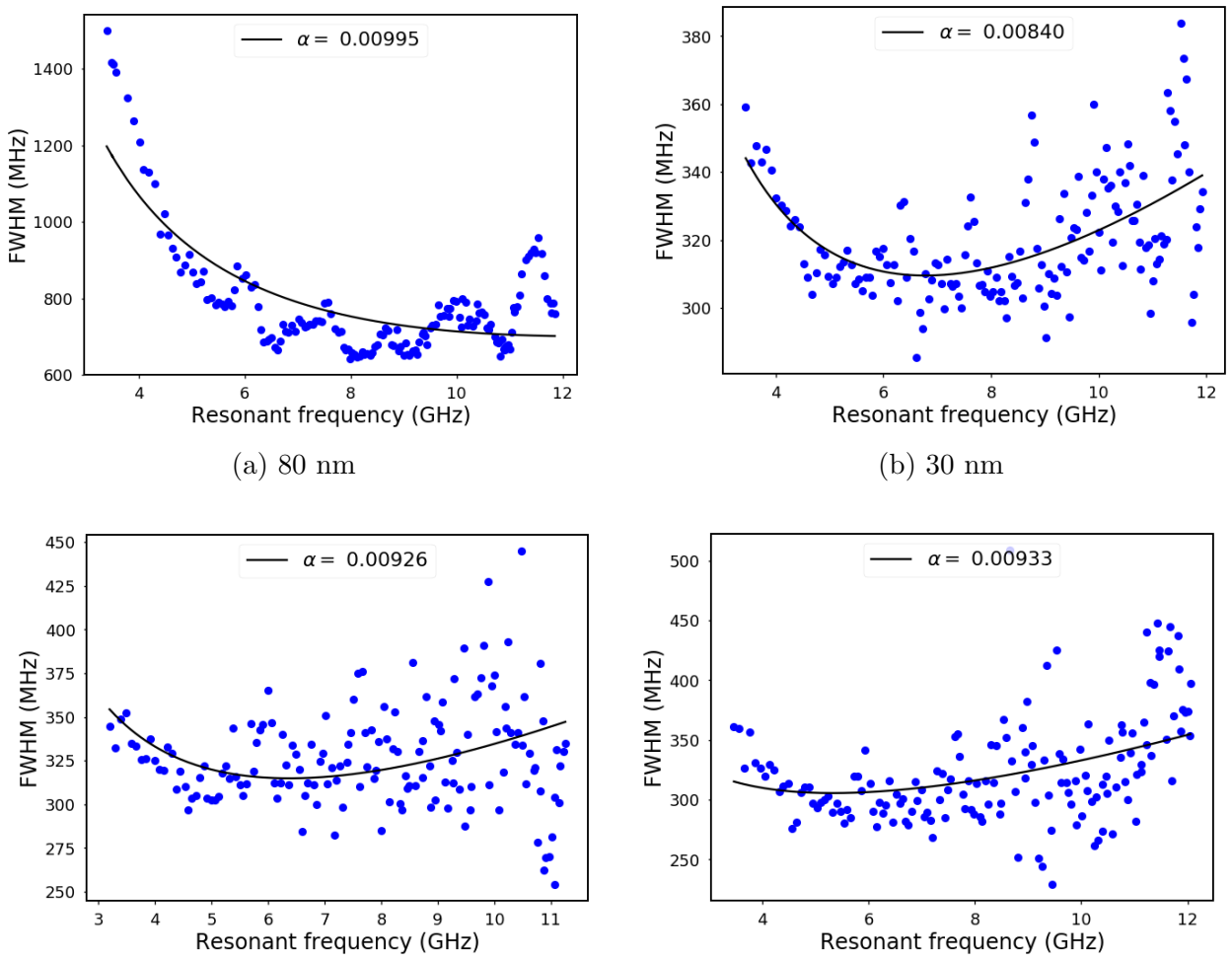

(a) 80 nm

(b) 30 nm

(c) 18 nm

(d) 10 nm

Figure 3.8: Frequency linewidth (FWHM) as a function of the resonance frequency from Fig. 3.7 for the Py(n)/SiO_2(0.25)/Si IP thickness series, for films of thicknesses **(a)** 80, **(b)** 30, **(c)** 18, and **(d)** 10 nm. The fit to Eq. 1.14 is plotted in black, and the extracted Gilbert damping α is displayed.

the 80 nm film, as does the extracted magnetization for the 80 nm film, $\boldsymbol{M}_S = 709.1$ kA/m. It is not clear why there is an almost 20% discrepancy between the measured magnetization and extracted magnetization, other than possible measurement error that could arise from a variety of sources (cabling, sample vibration, poor coupling, placement on the CPW, etc). Averaging over multiple sweeps could also correct the magnetization. However, the extracted value of $\boldsymbol{M}_s$ for the 10 nm Py film agrees with results in literature[37].

The FWHM is also extracted from the Lorentzian fit of the FMR signal at each magnetic field value, and this is plotted against the extracted resonant frequency for each film in Fig. 3.8. The linewidth curve is then fit to Eq. 1.14 to extract the Gilbert damping constant

α and the inhomogeneous linewidth ΔH_0 for each sample. The value of α is displayed for each film thickness. As summarized in Table 3.1, ΔH_0 is 922 A/m (11.6 Oe) and 962 A/m (12.1 Oe) for the 30 and 18 nm films, respectively, but is lower for the 10 nm film (555 A/m) and much higher for the 80 nm film (7490 A/m). Since this is a measure of the film's inhomogeneities, it is possible that the 80 nm film may be of worse quality than the others. Overall, though, the values of ΔH_0 are comparable to those found in some other studies of permalloy thin films[32].

The extracted α has an average standard deviation of 4% on the fit. The value of α is quite stable across film thickness, as shown in Fig. 3.15, being around 0.0085-0.009 for all films. This is above the typical intrinsic damping limit of $\alpha = 0.006$ for Py[5] [36] [38] [39], but is in the range of experimental values reported for Py films with thickness $d >= 30$ nm. Previous results have found a sharp increase in α for thicknesses below 10 nm[40], but show little thickness dependence above this value[38]. Thus, although the values of α are somewhat larger than usual, the lack of thickness dependence is expected given the larger thicknesses of the films.

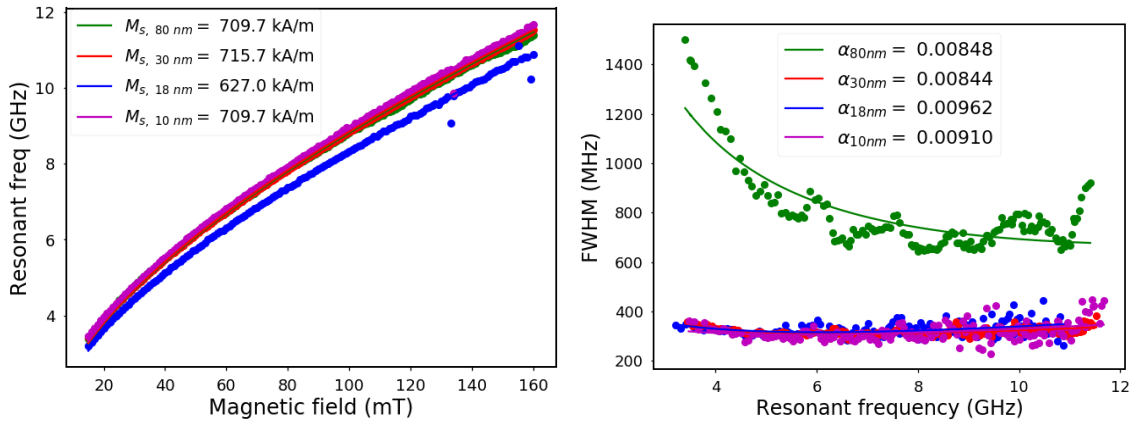

(a) (b)

Figure 3.9: **(a)** Resonance frequency as a function of magnetic field, swept from 15 mT to 160 mT, for the Py(n)/SiO_2(0.25)/Si IP thickness series, showing the fit to Eq. 1.10a and the extracted $\boldsymbol{M_s}$. The 18 nm sample, shown in blue, had a few incorrect fits (the dots separate from the main resonant frequency curve). **(b)** FWHM as a function of the fitted resonant frequency for the Py IP thickness series, showing the fit to Eq. 1.14 and extracted values of the Gilbert damping α.

The 80 nm film has dramatically larger frequency linewidth than the other samples. It also displays an unusual periodic variation of the linewidth with increased resonant frequency (Fig. 3.8a), while the other curves display more general variance about the fitted curve.

The resonance frequency and FWHM data, along with the fitted curves for each, are plotted together in Fig. 3.9 for quick comparison.

3.5 FMR in the out-of-plane orientation

The effectiveness of the flip-chip FMR setup was also tested in the OOP orientation, where the sample holder rod was rotated so that the waveguide plane was perpendicular to the external magnetic field, and the waveguide was placed so that the center conductor was oriented vertically, as shown in Fig. 3.2a.

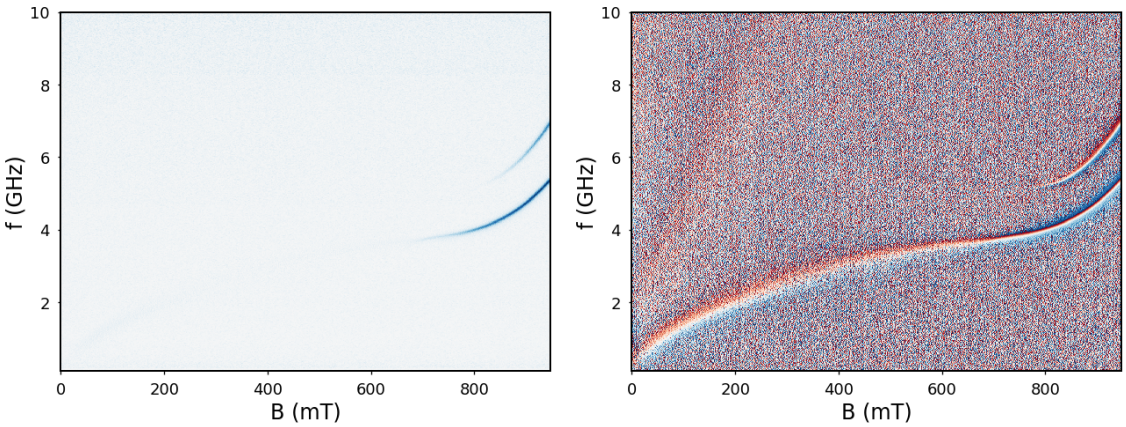

(a) (b)

Figure 3.10: Out-of-plane FMR sweep of 80 nm Py film on high-resistivity Si substrate, with in-plane easy axis. A second, higher-frequency spin-wave mode can be seen for this thicker film at high fields. **(a)** The magnitude of the resonant peak vs frequency and field. Darker blue lines indicates a stronger signal. **(b)** The phase of the resonant peak vs frequency and field. The red areas indicate a phase of $-\pi$, and the blue areas indicate a phase of $+\pi$. The white area transitioning from red to blue indicates a 2π phase shift, typical of resonance.

The same Py thickness series, despite having an in-plane magnetization, was measured in the OOP orientation, which is the sample's hard axis. When a magnetic film with a uniaxial anisotropy field H_u is biased along its hard axis, two resonance branches are seen, one at fields $H < H_u$, and the other at fields $H > H_u$ [41]. At this point, the bias field B_0 has overcome the anisotropy field $\mu_0 H_u$ to rotate enough of the spins to be parallel to the applied field, and resonance is dominated by this action along the hard axis. At high enough fields, all of the spins point along the hard axis, and the magnetization saturates in this direction.

Fig 3.10 shows the result of biasing the 80 nm Py film in the out-of-plane direction, and sweeping the field up to 1 T (the maximum field provided by the magnet). An IP resonance branch can be seen at lower fields, weak in magnitude (Fig. 3.10a) but clearly distinguishable by the 2π phase shift characteristic of FMR (Fig. 3.10b). Around $B_0 = 800$ mT, there is a transition to the second, much stronger (in terms of peak absorption) OOP resonance branch, showing the linear dependance on field as expressed in the Kittel equation (Eq. 1.10b). The transition to the OOP branch is complete by 900 mT. As seen in the VSM measurement in Fig. 3.6, the magnet is not saturated in the OOP direction until a field of

approximately 900 mT is applied, which corresponds to the results of the FMR sweep. The VSM measurement and FMR spectrum implies a value for the anisotropy field of $\mu_0 H_u \approx$ 800 mT, the point of the resonance transition. (A second, higher-frequency spin-wave mode is seen in the 30 nm and 80 nm films, above the resonance branch transition, and is visible in Fig 3.10. This mode is not present for the thinner films, with $d < 30$ nm).

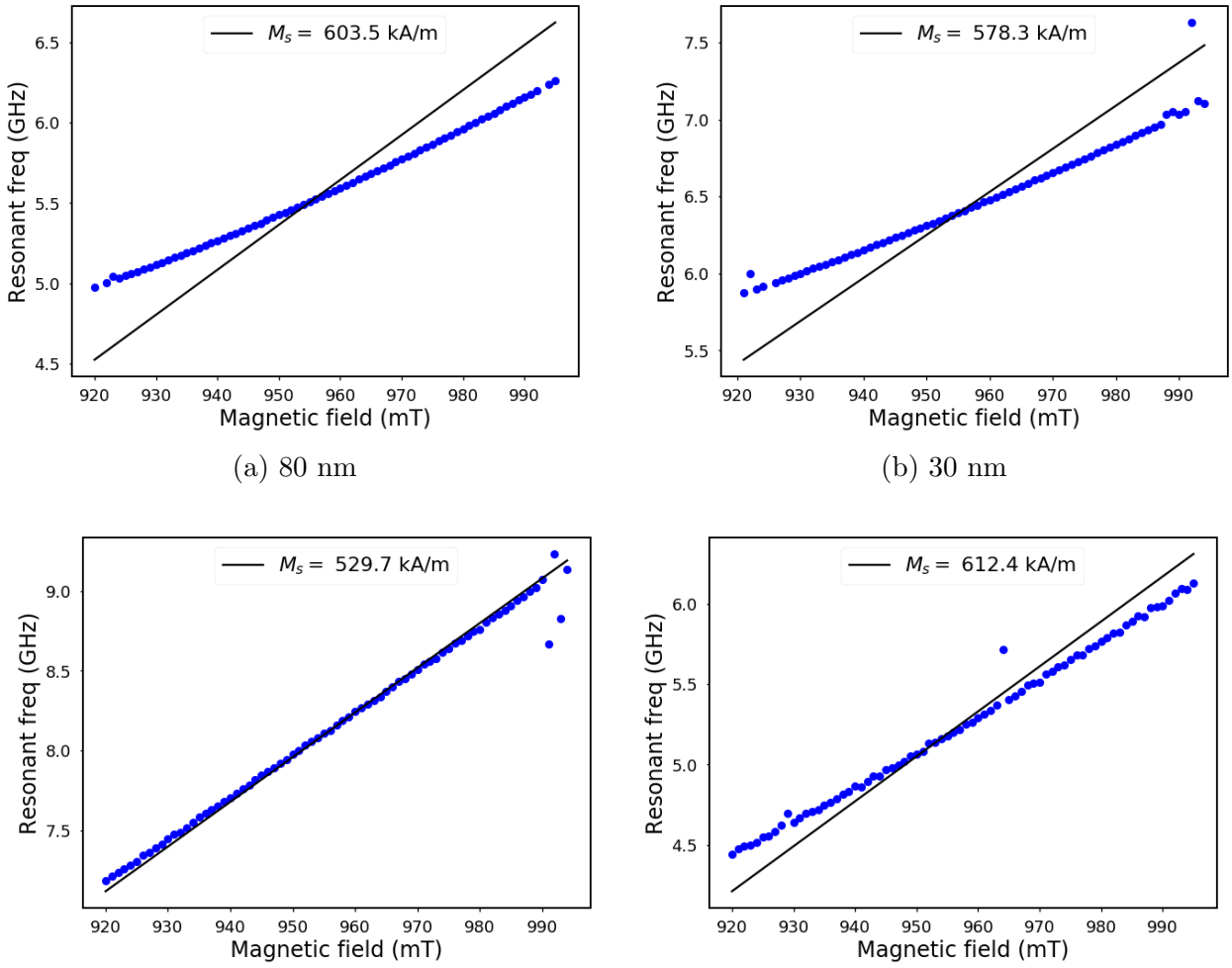

(a) 80 nm

(b) 30 nm

(c) 18 nm

(d) 10 nm

Figure 3.11: Resonance frequency as a function of magnetic field, swept from 920 to 995 mT, for the Py(n)/SiO_2(0.25)/Si OOP thickness series, for films of thicknesses **(a)** 80, **(b)** 30, **(c)** 18, and **(d)** 10 nm. The fit to Eq. 1.10b is plotted in black, and the extracted $\boldsymbol{M_s}$ is displayed.

Above the saturation field of $B_0 = 900$ mT, the magnetization is aligned along the hard axis and the Py behaves like a sample with out-of-plane magnetization. The resonance can then be analyzed using the OOP Kittel equation (Eq. 1.10b), and the film characteristics

can now be reanalyzed in this orientation. The resonance is fit from approximately 900 mT to approximately 1 T.

In Fig. 3.11, for each film thickness the resonance frequency for a given magnetic field has been found by fitting to a complex Lorentzian, and the resulting resonant frequency vs magnetic field curve has been found from a fit to Eq. 1.10b. The extracted $\boldsymbol{M}_s$ is displayed for each thickness. The value of the gyromagnetic ratio γ and Landé factor g was also found from this fit. g was found to be 1.948, 1.918, 2.0515, and 1.997 for the 80, 30, 18, and 10 nm films respectively (Table 3.1).

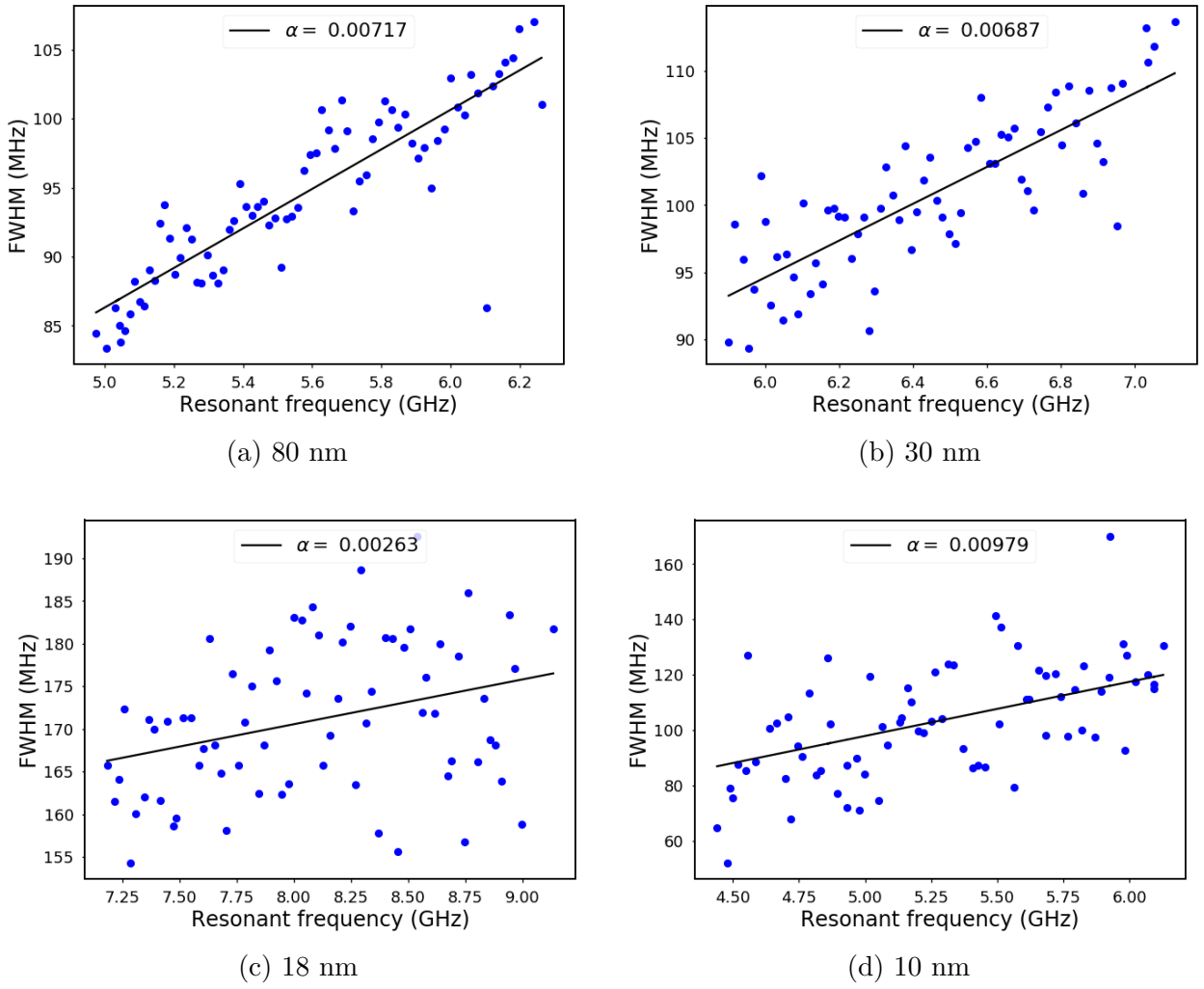

(a) 80 nm

(b) 30 nm

(c) 18 nm

(d) 10 nm

Figure 3.12: Frequency linewidth (FWHM) as a function of the resonance frequency from Fig. 3.11 for the Py(n)/SiO_2(0.25)/Si OOP thickness series, for films of thicknesses **(a)** 80, **(b)** 30, **(c)** 18, and **(d)** 10 nm. The fit to Eq. 1.14 is plotted in black, and the extracted Gilbert damping α is displayed.

The magnetization fit has a standard deviation of 0.1% on average. For the thicker films

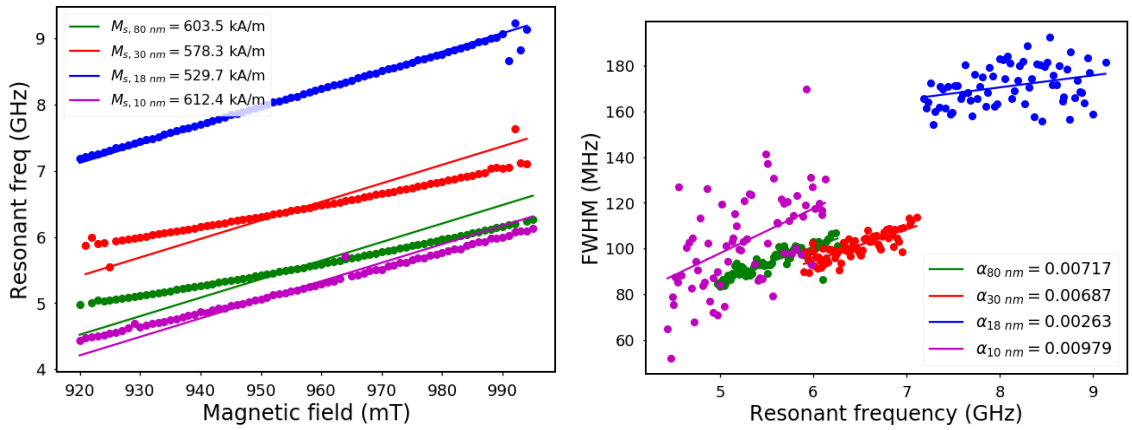

(a) (b)

Figure 3.13: **(a)** Resonance frequency as a function of magnetic field, swept from 920 mT to 995 mT, for the Py(n)/SiO_2(0.25)/Si OOP thickness series, showing the fit to Eq. 1.10b and the extracted $\boldsymbol{M_s}$. **(b)** FWHM as a function of the fitted resonant frequency for the Py OOP thickness series, showing the fit to Eq. 1.13 and extracted values of the Gilbert damping α.

the fitted curve appears to predict different resonant frequencies than were extracted; this is due to the limited fit area caused by the 1 T limit on the maximum field provided by the magnet. The extracted $\boldsymbol{M_s}$ for the 80 nm film agrees well with the value measured on the VSM. While the extracted magnetization was similar for all the film thicknesses for the IP case, in the OOP measurements $\boldsymbol{M_s}$ tended to decrease with film thickness. This is because the uniaxial anisotropy field H_u tends to increase as the film becomes thinner, which increases the frequency at which the resonance is seen and decreases the out-of-plane magnetization seen. The exception to this trend was the 18 nm film, which displayed an unusually high magnetization. This is most likely an anomalous result, considering that the 18 nm film was only measured once OOP, and considering that the film also displays unusual damping characteristics (see the next section).

The FWHM is also extracted from the Lorentzian fit of the FMR signal at each magnetic field value, and this is plotted against the extracted resonant frequency for each film in Fig. **??**. The linewidth curve, displaying a linear trend characteristic for OOP measurements, is then fit to Eq. 1.13 to extract the Gilbert damping constant α and the inhomogeneous linewidth ΔH_0 for each sample. The value of α is displayed for each film thickness.

The values of the inhomogeneous broadening ΔH_0 are generally better than for the IP measurements. As summarized in Table 3.1, ΔH_0 is 414 A/m (5.2 Oe), 126 A/m (1.58 Oe), and 176 A/m (2.21 Oe) for the 80, 30, and 10 nm films, respectively, but is much higher for the 18 nm film, 3626 A/m (45.56 Oe). The inhomogeneous field linewidth ΔH_0 is related to the inhomogeneous frequency linewidth by $\Delta H_0 = \gamma \mu_0 \Delta f_0$, and the resulting values of Δf_0 for the 30 and 10 nm films are comparable to those found for Py films biased OOP in

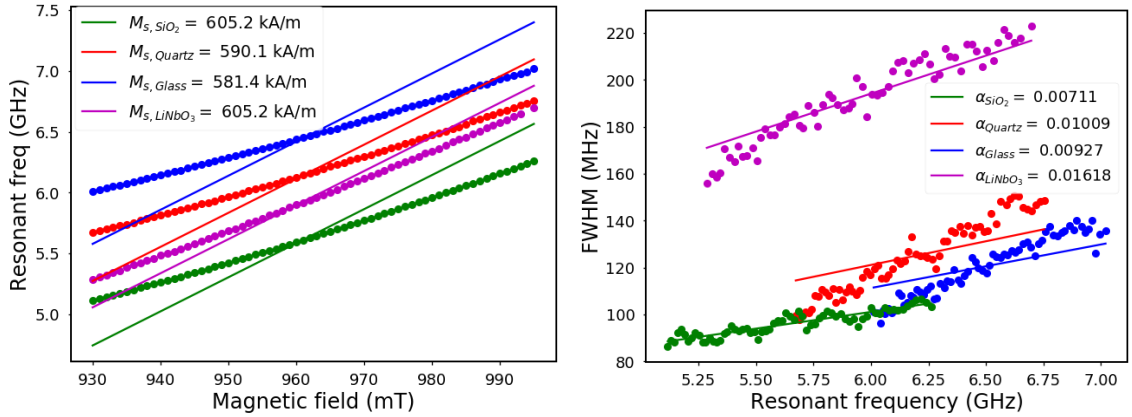

(a) (b)

Figure 3.14: **(a)** Resonance frequency as a function of magnetic field, swept from 930 mT to 995 mT, for 80 nm Py films on four different substrates in the out-of-plane orientation. The fit to Eq. 1.10a is shown, along with the extracted $\boldsymbol{M}_s$. **(b)** FWHM as a function of the fitted resonant frequency for the 30 nm Py out-of-plane substrate series, showing the fit to Eq. 1.14 and extracted values of the Gilbert damping α.

literature[30], indicating good homogeneity for those films. The large inhomogeneity of the 18 nm film suggests problems with the sample.

The value of α is generally stable across film thickness, as shown in Fig. 3.15, being around 0.007 for the thicker films (30 and 80 nm). This extracted value of alpha is typical for Py thin films in the out-of-plane direction [34]. For the 10 nm film, α is slightly larger, which is expected as it approaches the thin film limit. A large dip in α is seen for the 18 nm film, which might be related to the very large inhomogeneity of the sample. The out-of-plane resonance frequency and FWHM data, along with the fitted curves for each, are plotted together in Fig. 3.13 for quick comparison.

Out-of-plane FMR was also carried out for 80 nm Py samples on the four different substrates described in Sec. 3.3: high-resistivity Si, glass, $LiNbO_3$, and quartz. The extracted resonance and FWHM curves for the four substrates are shown in Fig. 3.14. While varying the thickness did not affect the extracted magnetization $\boldsymbol{M}_s$ or Gilbert damping α very much for the Py films, the choice of substrates did. This can be expected, as Gilbert damping is thought to arise from spin-lattice coupling, as discussed in Section 1.2, and so changing the crystal lattices and subsequent strains may affect the overall damping seen[42]. The high resistivity Si substrate displayed the lowest damping and smallest $\boldsymbol{M}_s$, while the piezoelectric $LiNbO_3$ substrate had dramatically enhanced damping, with an α almost twice that of the Si. The glass substrate displayed the lowest OOP $\boldsymbol{M}_s$, contributing to a higher resonant frequency for a given applied magnetic field. The higher damping found with the $LiNbO_3$ substrate is due to its magnetoelasticity, which contributes to a large spin-orbit coupling that increases its damping[43]. These results contributed to the decision to run all other

FMR sweeps of Py on high-resistivity Si substrates to achieve the lowest damping possible, close to the intrinsic damping limit for Py.

3.6 Summary of extracted constants

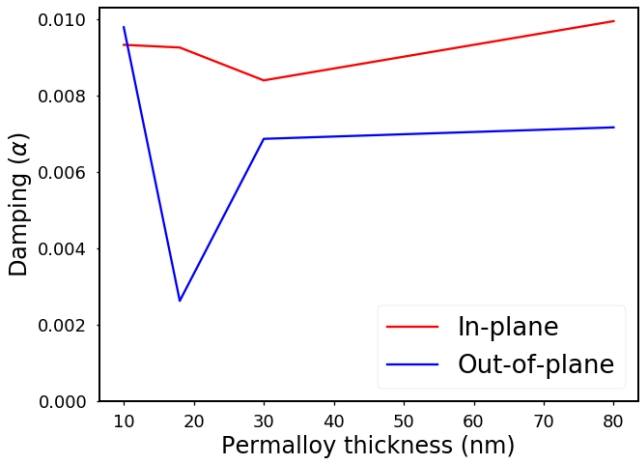

Figure 3.15: The Gilbert damping constant α as a function of the Py film thickness, evaluated at thickness t=10, 18, 30, and 80 nm. The red line indicates α for measurements done in-plane, while the blue line shows α for measurements done out-of-plane.

In previous sections, the extracted Gilbert damping constant α is displayed for the Py films measured in-plane and out-of-plane over 4 different thicknesses. The dependence of the damping constant on film thickness is summarized in Fig. 3.15 for IP and OOP measurements.

Table 3.1: Summary of parameters extracted from fit.

	Film thickness	**10 nm**	**18 nm**	**30 nm**	**80 nm**
In-plane	g	1.98	2.039	2.056	2.016
	M_s (kA/m)	$709.7 \pm 0.16\%$	$627.0 \pm 0.23\%$	$715.7 \pm 1.3\%$	$709.7 \pm 0.17\%$
	$\alpha(10^{-3})$	$9.10 \pm 3.51\%$	$9.62 \pm 2.57\%$	$8.44 \pm 1.3\%$	$8.48 \pm 8.61\%$
	ΔH_0 (A/m)	555	962	922	7490
Out-of-plane	g	1.947	2.0515	1.918	1.948
	M_s (kA/m)	$612.4 \pm 0.07\%$	$529.7 \pm 0.05\%$	$578.3 \pm 0.13\%$	$603.5 \pm 0.13\%$
	$\alpha(10^{-3})$	$9.79 \pm 20\%$	$2.63 \pm 38.9\%$	$6.87 \pm 6.98\%$	$7.17 \pm 6.48\%$
	ΔH_0 (A/m)	176	3626	126	414

Table 3.1 lists all the relevant FMR parameters extracted from the Py thickness series on high-resistivity Si substrate, as well as the standard deviation of the extracted $\boldsymbol{M_s}$ and α values to provide a sense of the error involved in the fits.

Chapter 4

Microwave probe FMR setup

While flip-chip is a standard measurement technique for conducting FMR, it has some limitations. The coupling between the magnetic film and the CPW is physically limited by the placement of the sample. In addition, the field lines generated by the RF current in the CPW are proportional in size to the width of the waveguide's center conductor. For very thin magnetic films, the coupling to a wide center conductor may be poor. Finally, as demonstrated in the previous chapter, a magnetic sample causes reflections by changing the characteristic impedance of the CPW, and the setup cannot be calibrated to remove losses through the soldered connectors.

Therefore, another method of VNA-FMR was sought that could allow for better CPW-to-magnet coupling and lower losses. In this chapter an FMR setup is presented that uses waveguides that have been deposited and lithographically patterned on top of the magnetic sample, and uses a microwave probe station together with the VNA to conduct the measurements. Section 4.1 describes the microwave probe station and new FMR setup, and compares it with the flip-chip setup described in Chapter 3. Section 4.2 describes the fabrication of CPWs on the surface of a magnetic sample. Finally, the setup is evaluated using the results of in-plane FMR sweeps on the same Py samples measured with the flip-chip setup. Although the microwave probe setup should theoretically provide better results than the flip-chip setup, issues with this measurement technique are described, and it is seen that absolute improvements in RF transmission do not necessarily produce a stronger FMR signal with higher SNR.

4.1 Microwave probe tip measurement and calibration

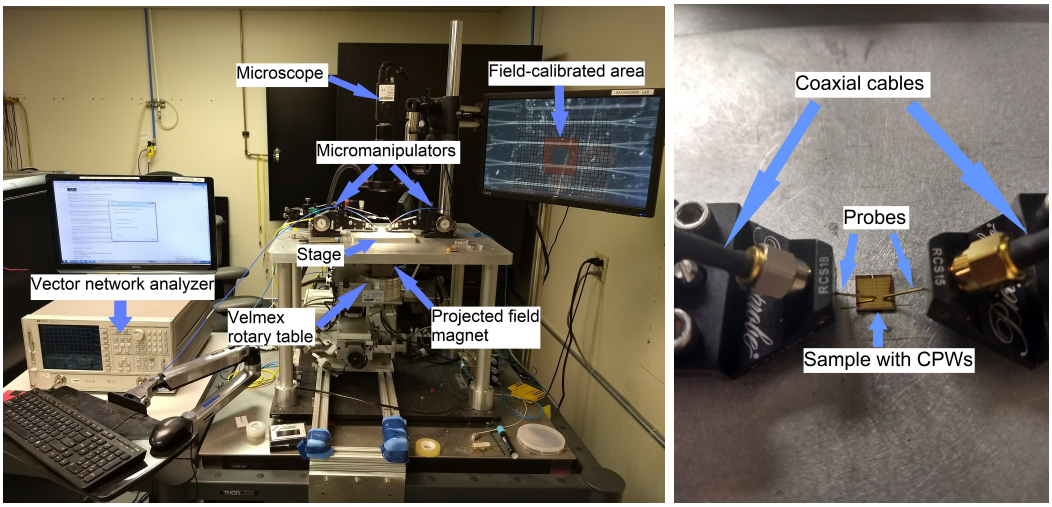

(a) (b)

Figure 4.1: **(a)** Microwave probe station setup with projected field magnet, VNA, probe tips, and sample loaded. **(b)** Closer view of microwave probe tips placed on pads at ends of the CPWs patterned on top of the magnetic sample.

A picture of the setup is shown in Fig. 4.1. It uses the same VNA and fitting software as the flip-chip setup, but instead of placing a CPW with sample between the poles of an external magnet, the CPW is placed on a probe station with a projected field magnet underneath. The magnet is mounted on a Velmex rotary table underneath the probe stage, and provides field uniformity over a small, calibrated area of the stage. The magnet sweep is controlled by a Kepco power supply, which sets the applied field. The magnetic sample, with the CPW deposited and patterned on top, is thus placed directly on the stage, with as little z-direction variation as possible to ensure uniformity (Fig. 4.1b), and with the area to be probed located within the calibrated area. The patterned CPW is small enough to fit within the calibrated area so the FMR sweep can have field uniformity. Since the magnetic field is projected in the xy direction of the stage, only in-plane FMR measurements can be conducted.

The two VNA ports are connected with SMA cables to microwave probes to provide RF signal to the CPW and measure the S_{21}. The microwave probe tips used were a GGB Industries Model 40A in the ground-signal-ground (GSG) configuration, with operation from DC to 40 GHz, mounted on MPH vacuum probe positioners from Cascade Microtech. The CPW must be designed so that the center conductor is wide enough for the signal tip to make contact, and to give the ground tips space on either side of the gaps.

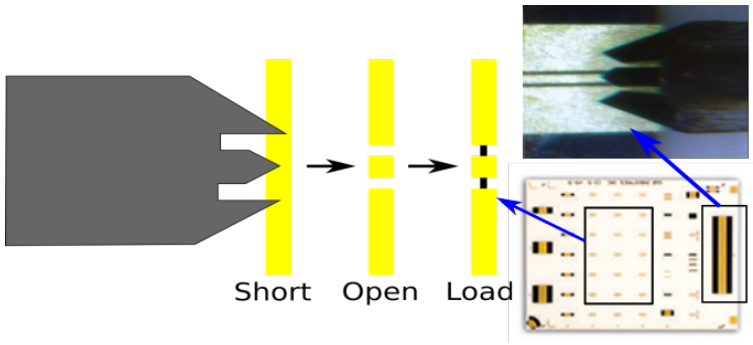

Figure 4.2: Illustration of the short-open-load-through procedure used to calibrate the microwave probe tips on a calibration substrate.

The short-open-load-through (SOLT) calibration procedure was used to calibrate the setup and remove noise found in the cables and probe tips. A calibration substrate was used, as illustrated in Fig. 4.2, consisting of a Short, with the signal line connected to ground; an Open, with the signal line separate from ground; a Load, with 50 Ω of resistance connecting the signal line and ground; and a Through, consisting of a CPW with 50 Ω characteristic impedance connecting the two probe tips for transmission calibration.

4.2 Fabrication details

CPWs were fabricated on top of magnetic chip samples with photolithography and thermal evaporation. The overall process is schematically illustrated in Fig. 4.3.

First, the sample chip is cleaned in acetone and isopropanol and purged in nitrogen, then subjected to a dehydration bake at 120 °C for 10 min. Next, the sample is coated in HMDS for 2 min to improve photoresist adhesion. It is then spincoated (5000 RPM, 30 s) with OCG 825 photoresist, a positive g-line photoresist. The sample is subjected to a softbake at 95 °C for 1 min 15 s, and then exposed to UV light through a chromium mask. Following exposure, the photoresist is developed with OCG 934 for 35 s. The development time is sharply defined by rinsing with de-ionized water for 30 s. Chromium and gold layers of 3 nm and 150 nm thickness, respectively, are deposited by thermal evaporation in a high vacuum chamber. The Cr layer is used as an adhesion layer for the Au. Finally, the metal is removed using the lift-off process by placing it in acetone to strip the photoresist, and placing the sample in a heated ultrasonic bath for 30 s. All steps are performed in a cleanroom with stable environmental conditions, except for the Py and capping layer deposition (sputtering described in Section 3.3).

The dehydration bake is crucial to remove any moisture from the surface of the sample, promoting photoresist adhesion and lift-off yield. While HMDS is not necessarily required to promote adhesion of photoresist to a Py surface with MgO capping layer, it is essential for adhesion to SiO_2 and other materials, and is thus used as part of the standard process

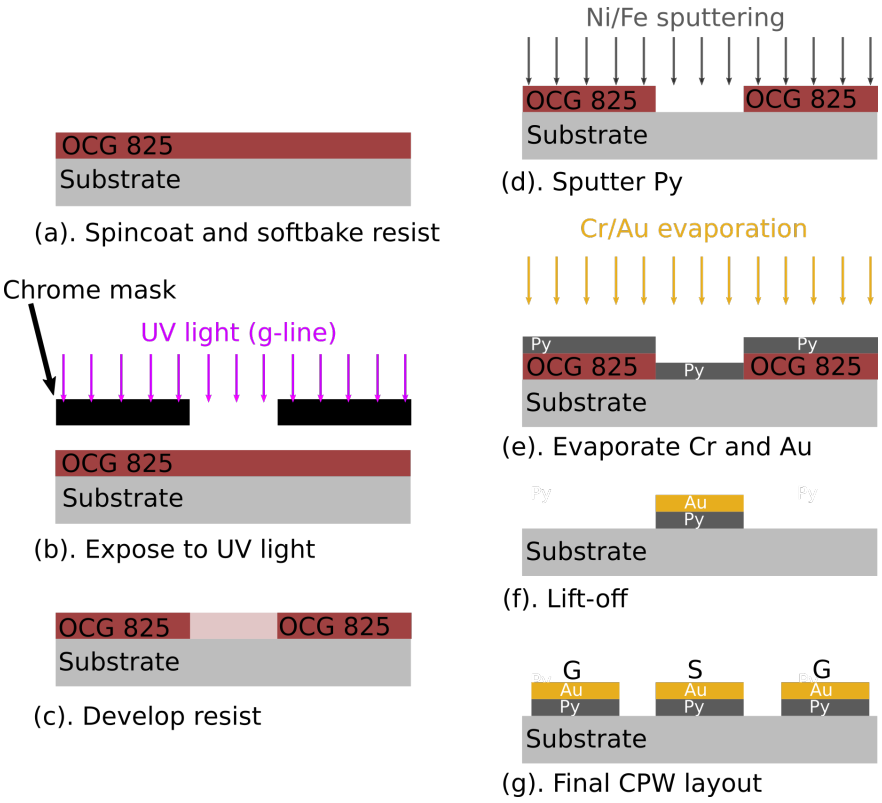

Figure 4.3: Photolithography steps for CPW patterning with lift-off. This specifically illustrates a process where lithography is done before Py deposition, but the magnetic layer may also be deposited before lithography and etched with an ion mill to provide isolation.

for FMR waveguide fabrication.

For a lift-off process with positive photoresist, the chromium mask was designed with negative polarity: that is, chrome was present in the CPW gap, so that photoresist will remain in the gap between the center conductor and waveguide, and remove any metal deposited on top of it in lift-off.

The process is flexible enough to deposit waveguides on a number of surfaces, including Si, SiO_2, capped Py, and Pt. The stack must have isolation between the CPW center conductor and ground planes to prevent shorting, which may be achieved a number of ways. A bare substrate may be patterned with photoresist, after which the magnetic material is deposited, followed by a capping layer, and finally the Cr/Au waveguide layer. The entire stack may then be lifted-off together, so that no Py remains in the CPW gap (Fig. 4.3). In this case, there is no direct isolation between the magnet and waveguide other than the thin capping layer. Alternatively, the magnetic layer may be deposited first, followed by lithography, Cr/Au deposition, and lift-off. If the 150 nm Au layer is significantly thicker than the magnetic layer (for thickness < 30 nm), the sample may be ion milled to remove the magnet in the gaps between the CPW signal and ground. The CPWs described here

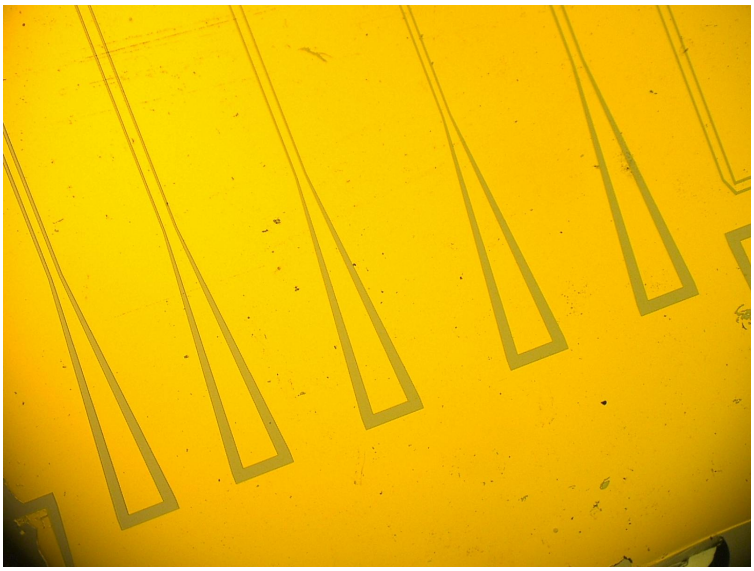

Figure 4.4: Microscopic image of a portion of the patterned Au waveguides on top of a Py sample after lift-off.

used the first approach, where lithography is done before the magnetic layer is deposited.

Overall, the process shows excellent uniformity due to the relatively large feature sizes used. Masks are designed to have a high density of CPWs to improve yield (Fig. 4.4), and the metal layers show good adhesion and thickness uniformity. The main concern is lithographic errors, cleanliness, and photoresist smudging. Since the CPWs tend to be fairly long (L=1000 μm for the standard design), there may be debris on the substrate or areas where the photoresist is smudged or removed. A single break in the center conductor will make the CPW unusable, and even slight variations in conductor width can change the impedance and increase loss. This problem can be minimized by using shorter waveguides so there is less chance of error at some point in the line. Density can also be improved with smaller CPWs, so yield overall goes up as the CPW length goes down.

4.3 Transmission comparison of CPW designs

The design of the lithographically patterned CPWs was detailed in Section 2.3, where the default dimensions were chosen to be $w_s = 20$ μm and $w_{sg} = 12$ μm, with L=1000 μm, and tapered RF pads of dimensions $w_s^{'} = 100$ μm and $w_{sg}^{'} = 58$ μm. On a 7.6 mm by 7.6 mm sample chip, there is sufficient space for many devices to be patterned at once to improve yield. In addition, to account for possible errors in calculation and to study the effect of dimension variation on performance, multiple CPW designs with different dimensions were put on the lithography mask in addition to the default design. The minimum feature width varied between 10 μm and 12 μm for various CPW designs.

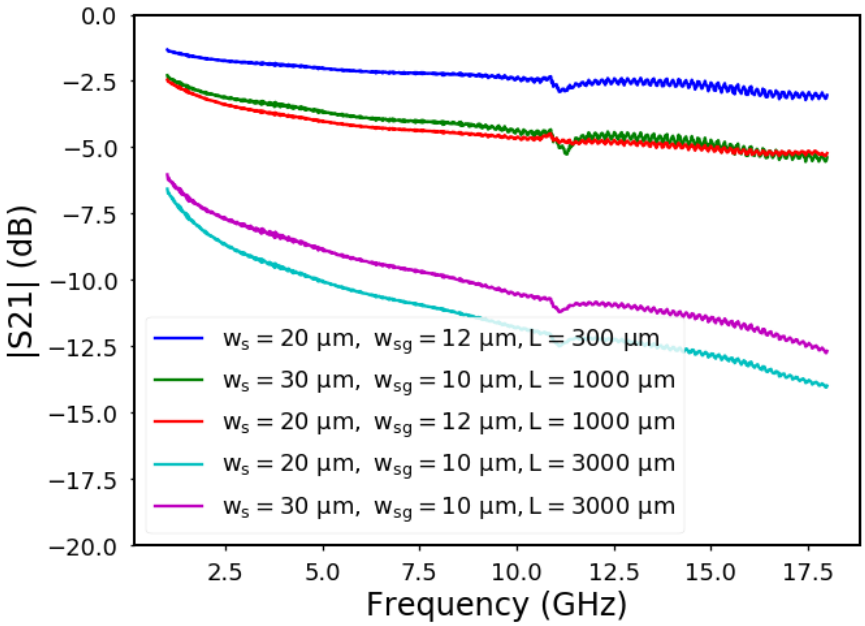

Figure 4.5: Magnitude of S_{21} (in dB) vs. frequency for patterned waveguides of different dimensions. Calibrated VNA measurement. The two CPWs with L=3000 μm are patterned on one sample, with the other three CPWs on a different sample. Amplitude ripple is visible for all CPWs, and it increases with frequency.

Fig. 4.7 shows the result of calibrated VNA measurements of five different CPW designs. In addition to the default waveguide with $w_s = 30$ 20 μm, $w_{sg} = 12$ μm, and L=1000 μm, a shorter CPW was measured with the same center conductor and gap dimensions but a length of L=300 μm. Two waveguides had $w_s = 30$ μm and $w_{sg} = 10$ μm, with lengths L=1000 and 3000 μm. Finally, a CPW was measured with $w_s = 20$ μm, $w_{sg} = 10$ μm, and L=1000 μm. The five CPWs were patterned on two separate Py(30)/high-resistivity Si samples. The two longer CPWs, with L=3000 μm were patterned on one sample, and the three shorter CPWs were on another.

If the metal is assumed to be a perfect, lossless conductor, the length of the line should not affect the impedance (except regarding quarter-wavelength effects at certain frequencies). Hence, L is not included in the analytic expression for Z_0 (Eq. 2.4). However, even in a good conductor like Au there is still attenuation due to its finite conductivity, as well as some variation across the sample or waveguide due to inhomogeneities or lithographic errors. In fact, S_{21} is seen to decrease with length for these CPWs, causing even more of an impact on transmission than the center conductor and gap width. When converted to impedance, the best performing CPW (with $w_s = 20$ μm, $w_{sg} = 12$ μm, and L = 300 μm) was measured to have $Z_0 \approx 46\ \Omega$. The longer waveguides with worse S_{21} were measured by the VNA to have $Z_0 \approx 38\ \Omega$, and correspondingly show higher S_{11} as well.

4.4 FMR measurements in probe station setup

Though the S_{21} varied from CPW to CPW, all of the FMR signals measured in the probe station setup had poor SNR, regardless of the CPW design. In fact, although CPW length negatively impacts S_{21}, it has little—or even opposite—effect on the strength of the FMR signal.

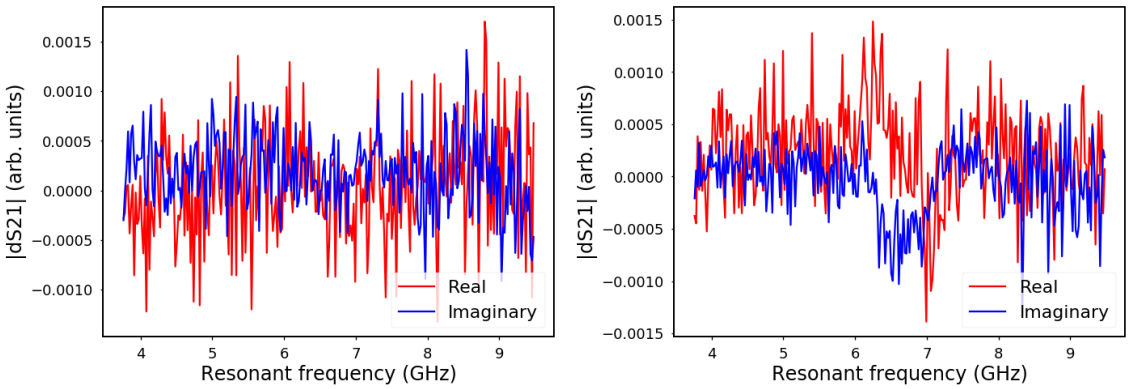

(a) (b)

Figure 4.6: FMR signal for 30 nm Py film at fixed magnetic bias ($B_0 = 76$ mT) as a function of frequency. **(a)** Measurement ran on CPW A ($w_s = 20$ μm, $w_{sg} = 12$ μm, and L=300 μm). CPW A had the highest S_{21} of all the CPWs. **(b)** Measurement ran on CPW B ($w_s = 20$ μm, $w_{sg} = 10$ μm, and L=3000 μm). CPW B had the lowest S_{21} of all the CPWs measured.

Fig. 4.6 compares the FMR signal vs frequency for two different CPW designs, both on 30 nm Py films and both at a field bias of $B_0 = 76$ mT. The measurement shown on the left (Fig. 4.6a) uses the "default" CPW that shows the best transmission ($w_s = 20$ μm, $w_{sg} = 12$ μm, and L=300 μm), that we shall call CPW A. The measurement shown on the right (Fig. 4.6b) uses the CPW with the worst S_{21} performance ($w_s = 20$ μm, $w_{sg} = 10$ μm, and L=3000 μm), that we shall call CPW B. CPW B has an S_{21} nearly 10 dB lower than CPW A across the entire operating range. Despite this, the FMR signal is actually weaker with CPW A; the resonance peak is barely visible. While both have very poor SNR, CPW A actually performs worse despite its better transmission.

In Section 3.2, it was shown that adding a constant offset to the S_{21} does not improve the FMR signal because FMR measures the change in S_{21}. Therefore, the absolute magnitude of S_{21} is unimportant. While CPW A shows better absolute magnitude, it has poor SNR because S_{21} still contains relatively large amplitude ripple. Amplitude ripple is the result of micro-reflections (due to impedance mismatch) creating standing waves on an RF line[44]. These standing waves cause both S_{11} and S_{21} to ripple. The amplitude ripple for CPW A can be seen in Fig. 4.7, reaching a magnitude of about 0.25 dB at higher frequencies.

If the amplitude ripple is larger than the change in absorption caused by FMR, the resonance signal will be overshadowed by the standing waves. Furthermore, because amplitude

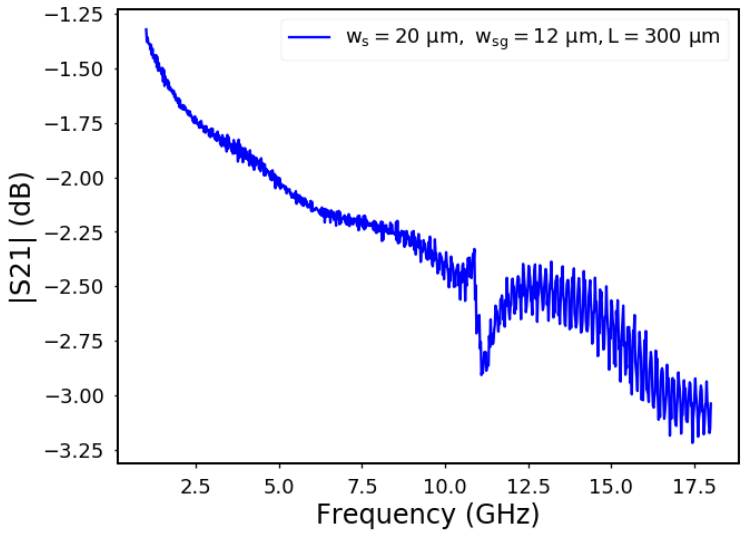

Figure 4.7: Magnitude of S_{21} (in dB) vs. frequency for "default" waveguide, with dimensions w_s = 20 µm, w_{sg} = 12 µm, and L=300 µm. Micro-reflections on the line cause amplitude ripple that increase with frequency.

ripple is the result of micro-reflections, it is not true "noise" and cannot be removed with averaging or lowering the IF bandwidth. Amplitude ripple is a particular problem for these lithographically patterned waveguides because the CPWs are so physically small that there is little magnetic material to change the absorption. For these CPWs, the change in absorption due to resonance is tiny because of the small number of magnetic moments. For this reason, even though CPW B (with L=3000 µm) has worse performance and larger amplitude ripple due to impedance mismatch, because it is ten times longer than CPW A (L=3000 µm), there is more magnetic moment to cause a larger change in absorption. As a result, the FMR signal is larger.

For these reasons, the FMR signal is consistently weak for measurements run with the microwave probe setup, despite the superior S_{21} performance over the flip-chip setup. The flip-chip setup has a larger CPW and uses the entire magnetic sample to cause a resonant change in absorption. To correct this problem, either the change in absorption at resonance must be enhanced or amplitude ripple must go down. Adding an RF attenuator should attenuate a micro-reflection every time it comes back to a port, damping out any standing waves, but this was unsuccessful in reducing the ripple. A matching network could be created to make sure that the CPW has a perfect impedance match to 50 Ω, although this may only cause matching at the CPW port, not throughout the entire line. The magnitude of the resonant absorption may be increased by increasing the size of the CPW so that it is coupled to more magnetic moments, but as mentioned before this hurts yield. Overall, the microwave probe setup needs further debugging and improvement before it can produce valuable measurements.

Chapter 5

Conclusion

In this report VNA-FMR is conducted in the frequency domain, as opposed to the more common field-swept FMR. CPWs were designed to provide an RF current for resonant excitation, and methods of effectively analyzing FMR signals and increasing signal strength are discussed. Two ferromagnetic resonance setups were designed, tested, and evaluated: one places a magnetic sample on top of the CPW in the flip-chip geometry, while the other probes CPWs that have been deposited on top of the sample.

The experimental design of the flip-chip setup is discussed first. To validate the setup, Py films of thickness 80, 30, 18, and 10 nm were measured in the in-plane (IP) and out-of-plane (OOP) orientations. Important magnetic parameters such as the saturation magnetization, Gilbert damping, and Landé g-factor were extracted, and found to be in reasonably good agreement with the expected values found in literature. Two resonant branches were observed when applying a magnetic bias along the Py hard axis, explained by a transition from IP to OOP FMR due to alignment of the magnetization with the external field. The choice of substrate is also found to substantially affect the magnetic parameters, with the magnetoelastic $LiNbO_3$ particularly enhancing damping. The microwave probe setup and a process flow for fabricating CPWs on top of a magnetic sample are described. The transmission properties of CPWs with different critical dimensions are compared, and the CPWs are found to have good RF performance. However, the resulting FMR signal is weak due to amplitude ripple caused by impedance mismatch, as well as the small amount of magnetic material available for resonance in the smaller, patterned CPW geometry.

Although permalloy is a well-studied magnetic material, the flip-chip FMR setup can be utilized to examine more novel magnetic materials. The setup is flexible enough to measure materials with an IP or OOP easy axis. Determination of these dynamic properties, particularly the damping, is critical to developing novel spintronic devices and manipulating spin currents and spin torques. While the microwave probe setup yields weak FMR signals, it can also easily be repurposed to conduct spin pumping experiments, which use a resonant ferromagnet as a source of spin current to measure the spin transport properties of ferromagnets/metal interfaces. Spin pumping can also be determined by the change in damping seen in ferromagnet/metal bilayers, so the flip-chip setup could be used for that purpose too.

Bibliography

[1] D. Griffiths, *Introduction to Quantum Mechanics*. Prentice Hall, 1995, pp. 160–162.

[2] F. Czeschka, "Spin Currents in Metallic Nanostructures," PhD thesis, Technische Universität München, 2011.

[3] X. Qiu, Z. Shi, W. Fan, S. Zhou, and H. Yang, "Characterization and Manipulation of Spin Orbit Torque in Magnetic Heterostructures," *Advanced Materials*, vol. 100, p. 1 705 699, 2018.

[4] D. Apalkov, B. Dieny, and J. M. Slaughter, "Magnetoresistive Random Access Memory," *Proceedings of the IEEE*, vol. 104, no. 10, pp. 1796–1830, 2016.

[5] G. Woltersdorf, "Spin-Pumping and Two-Magnon Scattering in Magnetic Multilayers," PhD thesis, Simon Fraser University, 2004, p. 22.

[6] S. Datta and B. Das, "Electronic analog of the electro-optic modulator," *Applied Physics Letters*, vol. 56, pp. 665–667, 1990.

[7] J. Atulasimha and S. Bandyopadhyay, *Nanomagnetic and Spintronic Devices for Energy-Efficient Memory and Computing*.

[8] T. Gilbert, "A phenomenological theory of damping in ferromagnetic materials," *IEEE Transactions on Magnetics*, vol. 40, p. 3443, 2004.

[9] J. Kuechle, "Broadband Ferromagnetic Resonance Setup," Bachelor's Thesis, Technische Universität München, 2015.

[10] M. Hickey and J. Moodera, "Origin of Intrinsic Gilbert Damping," *Physical Review Letters*, vol. 102, p. 137 601, 2009.

[11] K. Gilmore, Y. Idzerda, and M. Stiles, "Identification of the Dominant Precession-Damping Mechanism in Fe, Co, and Ni by First-Principles Calculations," *Physical Review Letters*, vol. 99, p. 027 204, 2007.

[12] L. Landau and E. Lifshitz, "On the Theory of the Dispersion of Magnetic Permeability in Ferromagnetic Bodies," *Physikalische Zeitschrift der Sowjetunion*, vol. 8, pp. 153–169, 1935.

[13] J.-M. Beaujour, W. Chen, K. Kryca, C.-C. Kao, J. Z. Sun, and A. D. Kent, "Ferromagnetic resonance study of sputtered Co— Ni multilayers," *The European Physical Journal B*, vol. 59, pp. 475–483, 4 2007.

[14] E. Barati, M. Cinal, D. Edwards, and A. Umerski, "Gilbert damping in magnetic layered systems," *Physical Review B*, vol. 90, p. 014 420, 2014.

[15] C. Kittel, *Introduction to Solid-State Physics*, 8th ed. John Wiley & Sons, 2005, pp. 380–381.

[16] S. Kalarickal, P. Krivosik, M. Wu, C. Patton, M. Schneider, P. Kabos, T. Silva, and J. Nibarger, "Ferromagnetic resonance linewidth in metallic thin films: Comparison of measurement methods," *Journal of Applied Physics*, vol. 99, p. 093 909, 2006.

[17] C. Patton, "Linewidth and Relaxation Processes for the Main Resonance in the Spin-Wave Spectra of Ni-Fe Alloy Films," *Journal of Applied Physics*, vol. 39, p. 3063, 1968.

[18] C. Bilzer, T. Devolder, J.-V. Kim, G. Counil, C. Chappert, S. Cardoso, and P. Freitas, "Study of the dynamic magnetic properties of soft CoFeB films," *Journal of Applied Physics*, vol. 100, p. 053 903, 2006.

[19] B. Kuanr, R. Camley, and Z. Celinski, "Narrowing of the frequency-linewidth in structured magnetic strips: Experiment and theory," *Applied Physics Letters*, vol. 87, p. 012 502, 2005.

[20] G. Counil, J.-V. Kim, T. Devolder, C. Chappert, K. Shigeto, and Y. Otani, "Spin wave contributions to the high-frequency magnetic response of thin films obtained with inductive methods," *Journal of Applied Physics*, vol. 95, p. 5646, 10 2004.

[21] J. Coonrod and B. Rautio, "Comparing Microstrip and CPW Performance," *Microwave Journal*, p. 76, 2012.

[22] M. El-Gibari and H. Li, "A Comparative Study between Via-Hole and Via-Free Grounded Coplanar Waveguide to Microstrip Transitions on Thin Polymer Substrate," *International Journal of Antennas and Propagation*, vol. 2015, 2015.

[23] D. Pozar, *Microwave Engineering*, 4th ed. John Wiley & Sons, 2012.

[24] G. Ghione and C. Naldi, "Coplanar Waveguides for MMIC Applications: Effect of Upper Shielding, Conductor Backing, Finite-Extent Ground Planes, and Line-to-Line Coupling," *IEEE Transactions on Microwave Theory and Techniques*, vol. 35, no. 3, pp. 260–267, 1987.

[25] B. Wadell, *Transmission Line Design Handbook*. Artech House, 1991.

[26] B. Rosas, *The Design and Test of Broadband Launches up to 50 GHz on Thin and Thick Substrates*. Southwest Microwave, 2011.

[27] V. Vlaminck, J. Pearson, S. Bader, and A. Hoffmann, "Dependence of spin pumping spin Hall effect measurements on layer thickness and stacking order," *Physical Review B*, vol. 88, p. 064 414, 2013.

[28] W. Zhang, M. Jungfleisch, W. Jiang, J. Sklenar, F. Fradin, J. Pearson, J. Ketterson, and A. Hoffmann, "Spin pumping and inverse spin Hall effects–Insights for future spin-orbitronics (invited)," *Journal of Applied Physics*, vol. 117, p. 172 610, 2015.

[29] I. Stanisopoulos, "Low damping and linearly polarized GHz magnetization dynamics in the chiral magnet Cu2OSeO3 hosting spin helices and skyrmions," PhD thesis, Technische Universität München, 2017.

[30] H. Maier-Flaig, S. Goennenwein, R. Ohshima, M. Shiraishi, R. Gross, H. Huebl, and M. Weiler, "Analysis of broadband ferromagnetic resonance in the frequency domain," *Journal of Applied Physics*, vol. 39, p. 3063, 2017.

[31] I. Neudecker, G. Woltersdorf, B. Heinrich, T. Okuno, G. Gubbiotti, and C. Back, "Comparison of frequency, field, and time domain ferromagnetic resonance methods," *Journal of Magnetism and Magnetic Materials*, vol. 307, pp. 148–156, 2006.

[32] T. White, "Ferromagnetic resonance to investigate spin pumping in permalloy multilayers," Master's Thesis, Rochester Institute of Technology, 2017.

[33] C. Bilzer, "Microwave susceptibility of thin ferromagnetic films: Metrology and insight into magnetization dynamics," PhD thesis, Université Paris Sud-Paris XI, 2007.

[34] M. Schoen, J. M. Shaw, H. Nembach, M. Weiler, and T. Silva, "Radiative damping in waveguide-based ferromagnetic resonance measured via analysis of perpendicular standing spin waves in sputtered permalloy films," *Physical Review B*, vol. 92, p. 184 417, 18 2015.

[35] R. Hertel, "Thickness dependence of magnetization structures in thin Permalloy rectangles: Dedicated to Professor Dr. Helmut Kronmüller on the occasion of his 70th birthday.," *Zeitschrift für Metallkunde*, vol. 93, pp. 957–962, 10 2002.

[36] C Luo, Z Feng, Y Fu, W Zhang, P. Wong, Z. Kou, Y Zhai, H. Ding, M Farle, J Du, and H. Zhai, "Enhancement of magnetization damping coefficient of permalloy thin films with dilute nd dopants," *Physical Review B*, vol. 89, no. 18, p. 184 412, 2014.

[37] D. Kim, H. Kim, C. You, and H. Kim, "Optimization of Ferromagnetic Resonance Spectra Measuring Procedure for Accurate Gilbert Damping Parameter in Magnetic Thin Films Using a Vector Network Analyzer," *Journal of Magnetics*, vol. 16, no. 3, pp. 206–210, 2011.

[38] Y. Zhao, Q. Song, S.-H. Yang, T. Su, W. Yuan, S. S. Parkin, J. Shi, and W. Han, "Experimental investigation of temperature-dependent gilbert damping in permalloy thin films," *Scientific reports*, vol. 6, p. 22 890, 2016.

[39] A Ghosh, J. Sierra, S Auffret, U Ebels, and W. Bailey, "Dependence of nonlocal gilbert damping on the ferromagnetic layer type in ferromagnet/cu/pt heterostructures," *Applied Physics Letters*, vol. 98, no. 5, p. 052 508, 2011.

[40] J. O. Rantschler, B. Maranville, J. J. Mallett, P. Chen, R. D. McMichael, and W. F. Egelhoff, "Damping at normal metal/permalloy interfaces," *IEEE Transactions on Magnetics*, vol. 41, no. 10, pp. 3523–3525, 2005.

[41] T. Vasilevskaya and D. Sementsov, "Ferromagnetic Resonance in a Uniaxial Magnetic Film Subjected to Magnetic Biasing along its Hard Axis," *Journal of Theoretical and Experimental Physics*, vol. 110, no. 5, pp. 754–758, 2010.

[42] N. Pertsev, H. Kohlstedt, and R. Knöchel, "Ferromagnetic resonance in epitaxial films: Effects of lattice strains and voltage control via ferroelectric substrate," *Physical Review B*, vol. 84, p. 014 423, 2011.

[43] S. Emori, B. A. Gray, H.-M. Jeon, J. Peoples, M. Schmitt, K. Mahalingam, M. Hill, M. E. McConney, M. T. Gray, U. S. Alaan, *et al.*, "Coexistence of Low Damping and Strong Magnetoelastic Coupling in Epitaxial Spinel Ferrite Thin Films," *Advanced Materials*, vol. 29, no. 34, 2017.

[44] R. Hranac, "What is a micro-reflection?" *SCTE Technical Columns*, 2009.